Flow phenomena and mechanisms in a field-scale experimental meandering channel with a pool-riffle sequence: Insights gained via numerical simulation

Seokkoo Kang[1] and Fotis Sotiropoulos[1]

Received 15 July 2010; revised 14 May 2011; accepted 23 May 2011; published 20 August 2011.

[1] Large-eddy simulation of turbulent flow through a natural-like meandering channel with pool-riffle sequences installed in the St. Anthony Falls Laboratory Outdoor StreamLab is carried out to elucidate the hydrodynamics at bankfull flow condition. It is shown that the shallow flow in the riffle is dominated by the presence of large-scale roughness elements that enhance turbulent mixing; increase turbulence anisotropy; and induce multiple, streamwise secondary cells driven by turbulence anisotropy. The flow in the pool, on the other hand, is dominated by the formation and interaction of the center region and outer bank secondary flow cells and the large horizontal recirculation regions along the inner bank. The collision of the counterrotating center region and outer bank cells at the water surface gives rise to a line of three-dimensional separation (flow convergence) in the time-averaged streamlines at the surface and the associated strong downward flow toward the bed that redistributes streamwise momentum and increases the bed shear stress along the channel thalweg. Intense turbulence is produced along the line of separation due to highly anisotropic velocity fluctuations. Our results make a strong case that the center region cell is driven by the curvature effects while the outer bank cell is driven by the combined effects of turbulence anisotropy and the curvature-induced centrifugal force. The inner bank horizontal recirculation zone consists of multiple eddies, which collectively span the entire point bar. A striking finding is that the center of the primary eddy is located directly above the crest of the point bar.

Citation: Kang, S., and F. Sotiropoulos (2011), Flow phenomena and mechanisms in a field-scale experimental meandering channel with a pool-riffle sequence: Insights gained via numerical simulation, *J. Geophys. Res.*, *116*, F03011, doi:10.1029/2010JF001814.

1. Introduction

[2] Meandering channels in nature consist of pool-riffle sequences [*Keller*, 1972; *Thompson*, 1986], which are the manifestation of rich morphodynamics emerging from the complex interaction of the turbulent flow with the streambed material. Riffles are typically shallow straight segments characterized by large water surface slopes, high velocities, and intense turbulent mixing. Pools, on the other hand, are characterized by larger depth, slower overall velocities and could exhibit significant longitudinal and transverse bathymetry gradients. The morphologic complexity of meandering streams gives rise to highly three-dimensional flows dominated by energetic coherent vortices, secondary flows, shear layers, regions of recirculation and flow stagnation, and pockets of highly nonisotropic turbulent stresses. It is presumably because of such complex flow phenomena and their poorly understood interactions with mobile streambeds that the underlying mechanisms that govern the formation of meanders in nature are still not entirely understood and cannot be fully explained by a single unifying theory [*Leopold and Wolman*, 1960; *Dietrich et al.*, 1979; *Frothingham and Rhoads*, 2003]. Yet understanding these mechanisms is critical prerequisite for developing physics-based approaches for stabilizing stream banks and restoring waterways. In this work we seek to contribute to this understanding by using high-resolution numerical modeling to elucidate the physics of several aspects of turbulent flows in a live-bed meandering channel with complex, albeit numerically fixed, bathymetry.

[3] One of the most important and well-known characteristics of flow through a meandering bend is the curvature-induced secondary motion that develops within the center region of the bend as the result of the imbalance of the centrifugal force and the transverse pressure gradient near the bed [*Van Bendegom*, 1947; *Rozovskii*, 1957; *Engelund*, 1974; *de Vriend*, 1977; *Humphrey et al.*, 1981; *Johannesson and Parker*, 1989]. This imbalance sets up a streamwise coherent vortical structure whose sense of rotation is such that it directs surface flow toward the outer bank and near-bed flow toward the inner bank. In this paper, we

[1]St. Anthony Falls Laboratory, Department of Civil Engineering, University of Minnesota, Minneapolis, Minnesota, USA.

0148-0227/11/2010JF001814

shall refer to this secondary cell as the center region cell. The center region cell has been studied extensively for well over a century due to its importance in redistributing momentum and transporting scalars (e.g., temperature) and sediments within the stream and its major role in determining stream morphodynamics [e.g., *Thomson*, 1876; *Kalkwijk and de Vriend*, 1980; *Dietrich and Smith*, 1983; *Johannesson and Parker*, 1989]. *Thomson* [1876], for instance, was the first to explain theoretically the occurrence of sediment deposition at the inner bank of the bend by linking this phenomenon to the center region cell and its propensity to transport sediment from the outer to the inner banks along the bed. *Kalkwijk and de Vriend* [1980] developed a mathematical model describing primary and secondary flow velocities in wide and mildly curved open channel bends while *Johannesson and Parker* [1989] developed a theoretical model for the calculation of secondary flow in mildly sinuous channels. *Blanckaert and de Vriend* [2003], *Bolla Pittaluga et al.* [2009], and *Blanckaert and de Vriend* [2010] also developed a mathematical model for primary and secondary flow in open channel bends. *Dietrich and Smith* [1983] studied the influence of the point bar on the flow in meander bends and found that its presence significantly modifies the flow patterns and the balance of the underlying hydrodynamic forces. They found the commonly assumed secondary flow pattern in the meander bend, which is outward flow at the surface and inward flow near the bed, does not occur over the entire cross section and there is an outward flow over the top of the point bar. *Frothingham and Rhoads* [2003] studied the three-dimensional flow structure and streambed change in an asymmetrical, compound meander loop by field investigation. They found that the helical mean flow motion associated with the center region cell decays rapidly as the flow moves toward inflections in curvature and that no mean streamlines complete a full cycle of helical rotation within a lobe. *Blanckaert* [2010] investigated the influence of the point bar on the flowfield and the underlying hydrodynamic forces using detailed laboratory measurements.

[4] The center region cell is often accompanied by a smaller secondary cell that rotates in the opposite direction and is located near the corner region between the water surface and the outer bank [*Bathurst et al.*, 1979; *Thorne et al.*, 1985]. This cell is known as the outer bank cell, and even though smaller and generally weaker than its center region counterpart, it is an important feature of meander bend flows as it can affect bank erosion processes by altering the streamwise velocity and boundary shear stress distributions. The outer bank secondary cell has also been the subject of extensive research through field investigations [*Hey and Thorne*, 1975; *Bathurst et al.*, 1979; *Thorne et al.*, 1985], laboratory experiments [*Blanckaert and Graf*, 2001; *Blanckaert and de Vriend*, 2004; *Jamieson et al.*, 2010] and numerical simulations [*van Balen et al.*, 2009; *Stoesser et al.*, 2010; *van Balen et al.*, 2010a, 2010b]. *Hey and Thorne* [1975] were among the first to observe that in natural rivers there exist two counterrotating secondary cells inducing water surface flow convergence, which gives rise to a vertical flow directed from the surface toward the bed and causes channel deepening. Subsequently, *Bathurst et al.* [1979] and *Thorne et al.* [1985] further reinforced the existence of the outer bank secondary cell in field studies. *Thompson* [1986] investigated the flow in a meandering gravel bed stream and observed a zone of upwelling adjacent to the outer bank of the stream and inward flow along the water surface toward a zone of convergence over the deepest part of the pool. To investigate the physical mechanisms that give rise to the outer bank cell in meander bends, *Blanckaert and Graf* [2001] and *Blanckaert and de Vriend* [2004] carried out detailed laboratory experiments in an open channel bend with mobile bed at resolution sufficiently fine to calculate the various terms in the budget of turbulence kinetic energy (TKE) and mean streamwise vorticity equations, respectively. They found that both the gradients of the cross-stream turbulent stresses and the centrifugal force contribute to the formation of the outer bank cell. *van Balen et al.* [2009] carried out large-eddy simulation (LES) to simulate the flow in a curved flume with rectangular cross section and confirmed that cross-stream turbulent stresses and centrifugal force play an important role in the formation of the outer bank cell. They also observed that the outer bank cell generates a pocket of increased TKE and TKE production. Moreover, *Blanckaert and de Vriend* [2004] and *van Balen et al.* [2009] also postulate that the low fluxes of kinetic energy from the mean flow to the turbulence play an important role in the generation of the outer-bank cell. *Stoesser et al.* [2010] employed both LES and Reynolds averaged Navier-Stokes (RANS) models with an isotropic turbulence closure to simulate the flow in a prismatic curved bend. They reported the isotropic RANS model failed to predict the outer bank cell. *van Balen et al.* [2010a] also carried out LES and RANS simulation for flow in strongly curved bend and compared results of both simulations. They reported the RANS model cannot reproduce the presence of the outer bank cell. The above mentioned numerical studies further reinforce the conclusion that turbulence anisotropy is a key contributor to the formation of the outer bank cell in curved open channels. In summary, the aforementioned studies make a strong case that the formation of the outer bank cell is driven by the combined effects of the centrifugal force and the anisotropy of turbulence. In spite of these important studies, however, the physics of the outer bank cell is, relative to its center region counterpart, not as well understood. This is especially true in natural meander bend geometries for which neither experiments nor simulations have been reported with resolution sufficiently fine to resolve the underlying physical phenomena and mechanisms with clarity.

[5] Another interesting phenomenon occurring in natural meander bend flows, which has not been studied as widely as the center region and outer bank cells, is the occurrence of horizontal flow separation at the inner bank of the bend. Several previous studies have observed occurrence of flow separation at the inner bank of natural or laboratory bends [*Bagnold*, 1960; *Leopold et al.*, 1960; *Leeder and Bridges*, 1975; *Nanson*, 1980; *Schmidt*, 1986; *Rubin et al.*, 1990; *Ferguson et al.*, 2003; *Blanckaert*, 2010]. *Bagnold* [1960] argued that flow separation occurs at the inner bank of the meander bend during the development of the bend creating deposition at the inner bank and its intensity reaches maximum for $r_m/w \simeq 2.0$, where r_m is the radius of curvature of the midstreamline and w is the width of the channel. *Leeder and Bridges* [1975] investigated flow separation in meander bends and related its occurrence to the bend tightness (r_m/w)

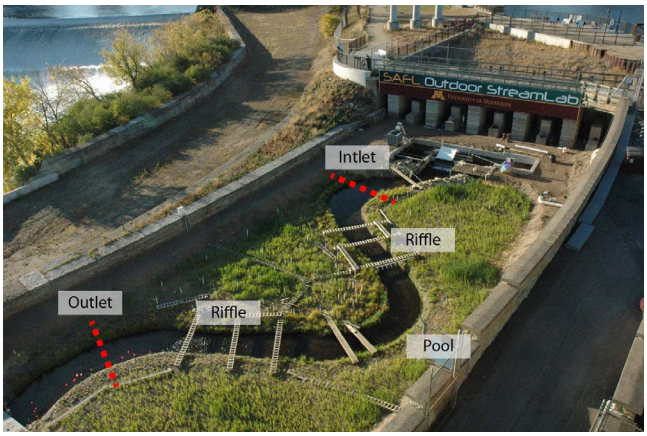

Figure 1. Outdoor StreamLab. Dashed lines indicate the inlet and outlet of the computational domain (image courtesy of Anne Lightbody).

and the Froude number. *Rubin et al.* [1990] observed recirculation zones and formation of bars in the Colorado River in the Grand Canyon and observed that deposition is focused at the separation point, reattachment point, recirculation eddy center, or along the shear surface that separates the recirculation zone from the faster moving flow in the main channel. *Schmidt* [1990] studied the formation of flow separation in the vicinity of a debris fan in the Colorado River in the Grand Canyon and found that recirculation zones increase in length with increasing discharge and that sandbars form beneath recirculation zones, especially near the separation and reattachment points. They also observed that the form and location of bars is consistent with the location and behavior of stagnation points in the river. *Ferguson et al.* [2003] carried out three-dimensional RANS simulations that solved flow in natural bends and observed the recirculation zone along the inner bank of the meander. They reported the slow flow at the inner bank recirculation zones can affect sediment dynamics by accumulating patches of fine sediment. Therefore, all previous field and laboratory studies indicate that flow separation occurring at the inner bank of the bend has a profound impact on meander morphodynamics as it is linked with the formation of bars at the inner bank of the bend.

[6] The above literature review highlights the complexity of meander bend flows and shows that even though significant progress has been made there are several aspects of such flows that are not entirely understood. One obvious limitation is that in field studies, that have yielded many of the insights reported above, the spatial and temporal resolution of streambed bathymetry and flow field measurements are inherently limited and, thus, are not sufficiently fine to elucidate physical phenomena and mechanisms with clarity. Laboratory studies and numerical simulations, on the other hand, are not constrained by such limitations but so far they have mostly focused on curved channels with simple (rectangular) cross-sectional shape or a simple planform with constant radius of curvature. The objective of this research is to contribute to the understanding of natural meander bend hydrodynamics via high-resolution numerical simulation using a recently developed LES model capable of simulating flows in arbitrarily complex natural streams [*Kang et al.*, 2011]. Specifically, we seek to elucidate the underlying physics of the mean flow and turbulence statistics in a field scale meander bend with emphasis on the structure, governing mechanisms, and possible influence on bed morphodynamics of key flow features such as the center region and outer bank cells and the horizontal recirculation regions along the inner bank. We also seek to explore the importance of turbulence anisotropy in various regions of the flow and discuss the implications of our findings for numerical modeling of such flows. A major difficulty for developing high-resolution computational models of natural meander bends stems from the aforementioned inherent measurement limitations in field experiments. To eliminate these difficulties we employ as the test case in this work the natural-like meandering channel in the St. Anthony Falls Laboratory Outdoor StreamLab (OSL), University of Minnesota, which is a field scale meandering channel research facility where experiments can be carried out under controlled conditions (see Figure 1). We employ high-resolution bathymetry measurements of the OSL streambed as input to the LES model previously developed and validated by *Kang et al.* [2011]. Note that in the work by *Kang et al.* [2011] we focused on the details of the numerical method and demonstrated its potential by applying it to calculate the base flow condition in the OSL using LES and unsteady RANS turbulence models. In this work we focus on the flow physics in the OSL at bankfull condition. We report additional validation of the LES model by comparing mean flow velocity and TKE profiles with measurements and analyze in depth the underlying flow phenomena and governing mechanisms in this field-scale natural-like stream.

[7] The paper is organized as follows. First, we present briefly the numerical model of *Kang et al.* [2011]. Subsequently, we describe the OSL facility and measurement techniques and discuss various computational details. This is followed by comparisons of the numerical solutions with measurements and extensive discussion of the simulated 3-D flowfields and underlying flow phenomena and mechanisms. Finally, we summarize the key conclusions of this work and discuss future research directions.

2. Numerical Method

[8] Even though numerical simulation of turbulent flows in natural rivers and streams has been the subject of intense research for well over fifteen years, to the best of our knowledge, coherent-structure resolving simulations of flows in geometries exhibiting the complexities that characterize natural waterways was only recently reported by *Kang et al.* [2011]. The method of *Kang et al.* [2011] is capable of simulating three-dimensional complex flows in arbitrarily complex domains with DNS, LES and URANS (unsteady RANS). The method employs the curvilinear immersed boundary (CURVIB) method proposed by *Ge and Sotiropoulos* [2007] to handle the presence of the highly complex bed topography that is characteristic of natural meander bends. Rather than using a boundary conforming mesh to describe the complex moving/stationary boundary, the CURVIB method treats the boundary as a sharp interface and boundary conditions are reconstructed at curvilinear grid nodes in the immediate vicinity of the boundary using interpolation along the local normal to the boundary direction

[*Gilmanov and Sotiropoulos*, 2005; *Ge and Sotiropoulos*, 2007]. The geometry of the natural meandering stream is first approximated by a meander bend of rectangular cross section that outlines and is sufficiently large to contain the entire natural streambed bathymetry at all locations. This approximate channel is discretized by a boundary-fitted curvilinear mesh and used as the background grid in the simulation. The measured natural bathymetry is then immersed in this background curvilinear grid and treated as a sharp-interface immersed boundary using the CURVIB approach. This approach is inherently suited for simulating natural streams of arbitrarily complex bathymetry even including complex instream structures. The details of the method can be found in the work of *Kang et al.* [2011]. Here we only present a brief summary of the overall numerical method.

2.1. Resolved Flow Equations

[9] The equations governing the instantaneous, resolved flowfield for three-dimensional, incompressible, turbulent flow are the spatially-averaged continuity and Navier-Stokes equations. In the CURVIB method of *Ge and Sotiropoulos* [2007] the governing equations are first written in Cartesian coordinates $\{x_i\}$ and then transformed fully (both the velocity vector and spatial coordinates are expressed in curvilinear coordinates) in nonorthogonal, generalized, curvilinear coordinates $\{\xi^i\}$. The transformed continuity and momentum equations read in compact tensor notation (repeated indices imply summation) as follows ($i, j = 1, 2, 3$):

$$J\frac{\partial U^j}{\partial \xi^j} = 0, \tag{1}$$

$$\begin{aligned}\frac{1}{J}\frac{\partial U^i}{\partial t} = &\frac{\xi_l^i}{J}\left(\frac{\partial}{\partial \xi_j}\left(U^j u_i\right) + \frac{1}{\rho}\frac{\partial}{\partial \xi_j}\left(\mu\frac{g^{jk}}{J}\frac{\partial u_i}{\partial \xi_k}\right)\right.\\ &\left. - \frac{1}{\rho}\frac{\partial}{\partial \xi_j}\left(\frac{\xi_i^j p}{J}\right) - \frac{1}{\rho}\frac{\partial \tau_{ij}}{\partial \xi_j}\right),\end{aligned} \tag{2}$$

where J is the Jacobian of the geometric transformation $J = |\partial(\xi^1, \xi^2, \xi^3)/\partial(x_1, x_2, x_3)|$, $\xi_j^i = \partial\xi^i/\partial x_j$ are the transformation metrics, u_i is the filtered ith Cartesian velocity component, $U^i = (\xi_m^i/J)u_m$ is the filtered contravariant volume flux, $g^{jk} = \xi_l^j\xi_l^k$ are the components of the contravariant metric tensor, p is the pressure, ρ is the density, μ is the dynamic viscosity, and τ_{ij} is the subgrid stress (SGS) tensor for LES. The SGS tensor is closed using the dynamic Smagorinsky model [*Germano et al.*, 1991] as described in detail by *Kang et al.* [2011].

[10] The governing equations, equations (1) and (2), are discretized in space using three-point central, second-order accurate finite differences for all spatial derivatives. The temporal discretization is fully implicit with second-order backward differencing for the time derivative term in the momentum equations. The discrete equations are integrated in time using a fractional step method with matrix-free Krylov-based solvers for the momentum and pressure equations. The efficiency of the pressure equation solver is further enhanced by employing the algebraic multigrid method, which was shown [*Kang et al.*, 2011] to significantly improve the computational efficiency of the numerical solver in problems involving a long and high-aspect ratio computational domain such as those encountered in natural meander bends.

2.2. Near-Wall Boundary Conditions

[11] In high Reynolds number flow simulations, applying the no-slip boundary condition at the wall is often impractical as excessively fine meshes and long computational times would be required for accurate implementation. To address this difficulty in this work we employ the wall model proposed by *Cabot and Moin* [2000] and *Wang and Moin* [2002]. The model solves the boundary layer equation in the following form:

$$\frac{1}{\rho}\frac{\partial}{\partial n}\left((\mu+\mu_t)\frac{\partial u_s}{\partial n}\right) = \frac{1}{\rho}\frac{\partial p}{\partial s} + \frac{\partial u_s}{\partial t} + \frac{(\partial u_n u_s)}{\partial n}, \tag{3}$$

where n and s indicate the directions normal and tangential to the wall, respectively. By neglecting the right-hand side of equation (3), one obtains the equilibrium stress balance model [*Wang and Moin*, 2002]

$$\frac{1}{\rho}\frac{\partial}{\partial n}\left((\mu+\mu_t)\frac{\partial u_s}{\partial n}\right) = 0. \tag{4}$$

The eddy viscosity is given by the mixing length model with the near-wall damping as follows:

$$\mu_t = \mu\kappa n^+\left(1 - e^{-n^+/19}\right)^2, \tag{5}$$

where $n^+ = \rho u_\tau n/\mu$, and u_τ is the wall shear velocity. Equation (4) is integrated from the wall of the immersed body to the second off-wall node to obtain the velocity at the first off-wall node. The implementation of this model in the context of the CURVIB method is described in detail by *Kang et al.* [2011].

3. Test Case and Computational Details

3.1. The St. Anthony Falls Laboratory Outdoor StreamLab

[12] The St. Anthony Falls Laboratory Outdoor StreamLab (OSL) (Figure 1), located at University of Minnesota, Minneapolis, Minnesota, USA, is a field-scale research facility, which during 2008 was configured into a meandering channel with a pool-riffle sequence. The research facility is a 40 m by 20 m basin, which has been configured into a sand-bed meandering stream channel with a pool-riffle sequence that is approximately 50 m long, 3 m wide, and 0.3 m deep at bankfull flow. The wavelength of the meander is approximately 25 m, and the channel was laid out as a sine-generated curve with moderate sinuosity (equal to 1.3). The maximum values of flow depth and the channel width at the apex of the bend are 0.37 m and 3.3 m, respectively. Figure 2 shows the longitudinal profiles of the measured water and bed elevations in the OSL. Native riparian seedings were planted along the stream bank during the first year of operation (2008) along with biodegradable coconut-fiber bank stabilization matting. By 2009, the vegetation had established stable root systems that, along with the remains of the initial coconut fiber matting, stabilized the bank position. Due to the bank stabilization matting and the vegetation, the stream bank of the OSL was

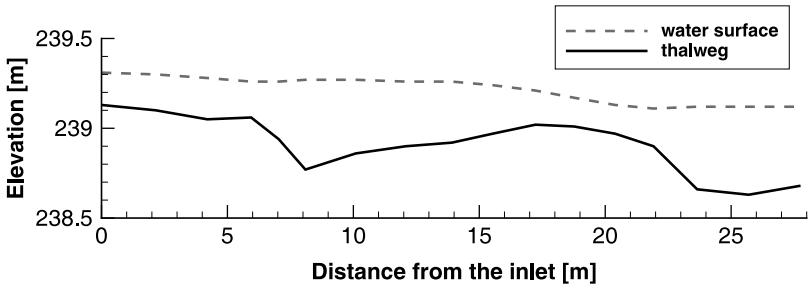

Figure 2. The longitudinal profiles of water and bed elevations measured along the centerline and the thalweg of the OSL, respectively.

protected from erosion. We note that the effect of the stream bank vegetation was neglected in our simulation. The floodplain was seeded with a mixture of native prairie grass seed. Entrance conditions for the OSL allow accurate control and measurement of water and sediment discharge rates, and the facility is outfitted with a sedimentation basin at its downstream end where sediment is collected and stockpiled for recirculation. Simulations and measurements reported herein were performed for a flow rate of 2.85×10^{-1} m^3/s, which yields Reynolds and Froude numbers, based on depth and velocity at the inlet, approximately equal to 10^5 and 0.4, respectively. Various relevant hydraulic and geometric parameters are summarized in Table 1. The mean sediment feed rate at the inlet was approximately 4 kg/min, and the median grain size of the sediment fed into the channel was 0.7 mm. The bed materials in the riffles consist of gravel ranging from 10 cm to 15 cm in length, which is large enough to withstand the maximum bed shear stress and as a result the riffle topography was mostly fixed. The bed in the pool was initially constructed with a flat sand bed and was allowed to evolve naturally toward a quasi-equilibrium state, with point bars and deep pool regions along the inner and outer banks, respectively, as described below.

[13] Three-dimensional mean velocity and turbulence statistics measurements in the OSL were obtained using acoustic Doppler Velocimetry (ADV; Nortek Vectrino) at 50 Hz for 5 minutes at each location. The ADV probes were mounted to a channel-spanning portable traverse enabling lateral and vertical positioning. At each cross section, the position of this traverse was recorded using a total station (Sokkia X30RK), enabling registration of each sampling location within a common coordinate system. ADV measurements were obtained at four channel cross sections located throughout the length of the channel: one across the midpoint of each riffle section and two throughout the middle meander bend. At each cross section, vertical profiles were sampled every 0.25 m laterally at 0.05 m vertical spacing between sampling positions.

[14] Bed and water surface topography in the OSL were collected on a 1 cm horizontal grid at submillimeter vertical accuracy using instruments mounted to a separate channel-spanning portable carriage, the position of which was registered using the total station. A laser distance sensor (Keyence LK-G series) was used for collecting subaerial bank topography, while a pulser and ultrasonic submersible transducer system (JSR Ultrasonics) documented subaqueous topography. Mean water surface elevation measurements were sampled at 50 Hz over a centimeter-scale spaced grid using an ultrasonic distance sensor (Massa).

[15] The OSL was first run with the given discharge for several days until the bed in the pool region does not change significantly over time. Subsequently the water and bed surfaces were measured and velocity data were collected for several weeks throughout the channel. Because of the limited window size of the bed topography scanner the channel was divided into many regions where the bed elevation was measured during different times. In each region, bed and water surfaces measured for a finite time and averaged in time in order to obtain input data for the computation. The obtained bed topography in each measurement window was assembled together to form a single bed topography shown in Figure 3. During the time of the measurements a long-term morphological change was observed in some regions of the pool, and this was not accounted in the time-averaged bed topography. We note, however, that the long-term variability of the bed elevation in some regions was not negligible, and thus nonsmooth bed topography inevitably existed at the interface between the different measurement windows that were assembled together to construct the channel bathymetry seen in Figure 3. Particularly, there exist noticeable discontinuities of the bed topography near the interface between the first riffle zone and the following pool zone. These errors in the topography may well affect the accuracy of the calculated local flowfield but as we will subsequently show, the overall pattern of mean velocities and large scale motions are not significantly influenced by those errors.

[16] It is also important to note that during the experimental runs, fast-moving ripples or dunes were observed near the bed of the pool regions. No attempt was made to quantify experimentally the height and length of such fast-moving bed forms and for that their existence was not taken into account in the numerical simulation, which, as discussed above, employed the time-averaged measured bed elevation as input. This simplification prevents us from

Table 1. Hydraulic and Geometric Parameters of the Bankfull Flow in the OSL[a]

Q	Re	Fr	D	B	S
2.85×10^{-1} m^3/s	10^5	0.4	0.3 m	3 m	0.01

[a] Q is mean flow rate, Re is Reynolds number, Fr is Froude number, D is mean flow depth, B is mean channel width, and S is mean bed slope.

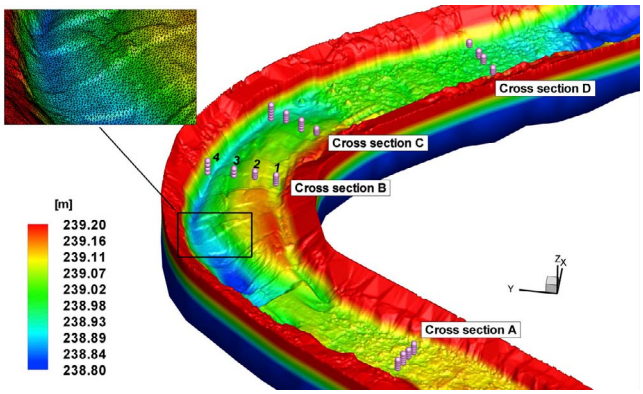

Figure 3. The SAFL Outdoor StreamLab bathymetry obtained from high-resolution measurements. The streambed is discretized using 236,370 triangular elements and treated as an immersed boundary. The contour levels denote bed elevations. The symbols and numbers mark velocity measurement locations. The flow direction is from bottom to top.

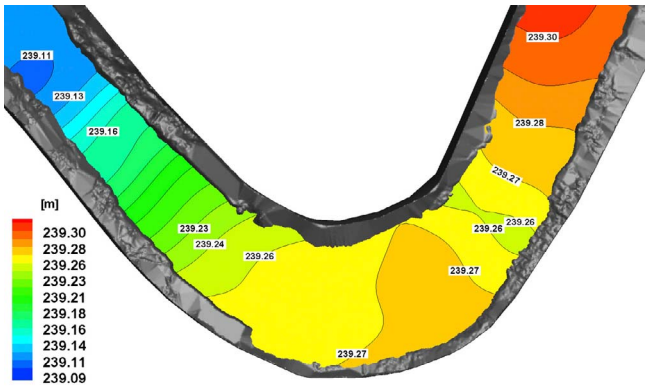

Figure 5. Water surface elevations used to define the rigid lid upper boundary in the computational model (the contour levels denote the water surface elevations; flow is from right to left). The elevations are interpolated from the measurements.

studying the effect of dynamic bed forms on streambed roughness.

3.2. Computational Setup

[17] The immersed body that represents the bed topography was constructed from the measured time-averaged bed topography data (see Figure 3), which was assembled by stitching together the time-averaged bathymetry obtained in the various measurement windows as previously described. The aforementioned bathymetry discontinuities at the interfaces of various windows were retained in the simulation as no attempt was made to smooth the overall measured data. The so resulting bed geometry is discretized with 236,370 triangular elements as required by the CURVIB method (see *Kang et al.* [2011] for details). The size of the bathymetry mesh is small enough to resolve individual bed roughness in the riffle zones. The body-fitted curvilinear grid that discretizes the rectangular meandering channel (see *Kang et al.* [2011] for details) that contains entirely the natural OSL bathymetry consists of 2001 × 241 × 101 grid points in streamwise, transverse, vertical directions, respectively, and which approximately follows the meander of the channel. The total number of the grid points is about 49 million with approximately 15 million and 34 million cells located in the fluid and solid phases, respectively. The grid spacing in the streamwise, transverse and vertical directions is about 2.0 cm, 1.5 cm and 6 mm, respectively. The grid nodes are uniformly distributed in the vertical direction and an orthogonal curved grid is used in the horizontal plane. In summary, the 30 m long, 3.5 m wide and 0.6 m high background computational grid, which surrounds the channel, is filled with 49 million cells with the size of 2.0 cm × 1.5 cm × 6 mm. The streamwise, transverse and vertical grid spacing correspond to approximately 400, 300 and 140 wall units, respectively, based on the measured mean bed shear stress. Figure 4 shows the computational grids at a cross section in the pool and a vertical plane 2 cm above the mean bed elevation in the second riffle.

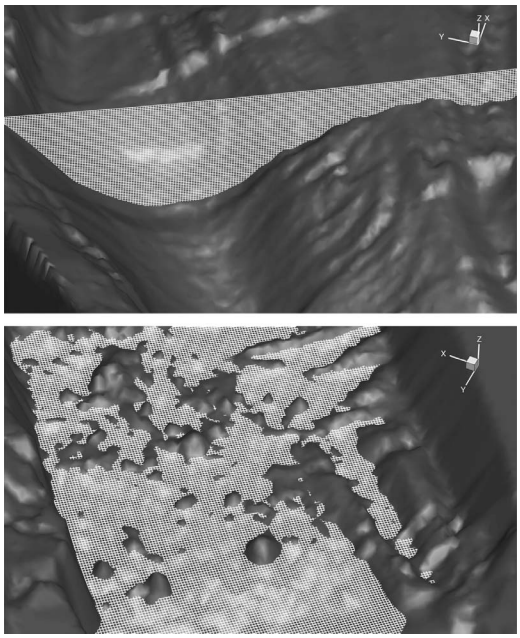

Figure 4. Typical views of (top) the background computational grid at a cross section in the pool and (bottom) a horizontal plane 2 cm above the mean bed elevation in the second riffle (flow is from bottom to top).

[18] The measured time-averaged free surface elevation (see Figure 5) is used to prescribe the water surface, and no-flux and free-slip boundary conditions are employed for the instantaneous velocity field. The unsteady turbulent inflow condition, which was extracted from the separate LES solving the fully developed open channel flow with streamwise periodicity, is specified at the inlet. The separate LES for the generation of the inlet velocity boundary condition was carried out before running the main simulation. Instantaneous three-dimensional velocity fields at the selected cross section were stored over a time interval of 40,000 time steps. These velocity time series were fed into the inlet of the main computational domain by recycling them every 40,000 time steps. The wall model proposed by *Kang et al.* [2011] is used to compute the velocity boundary

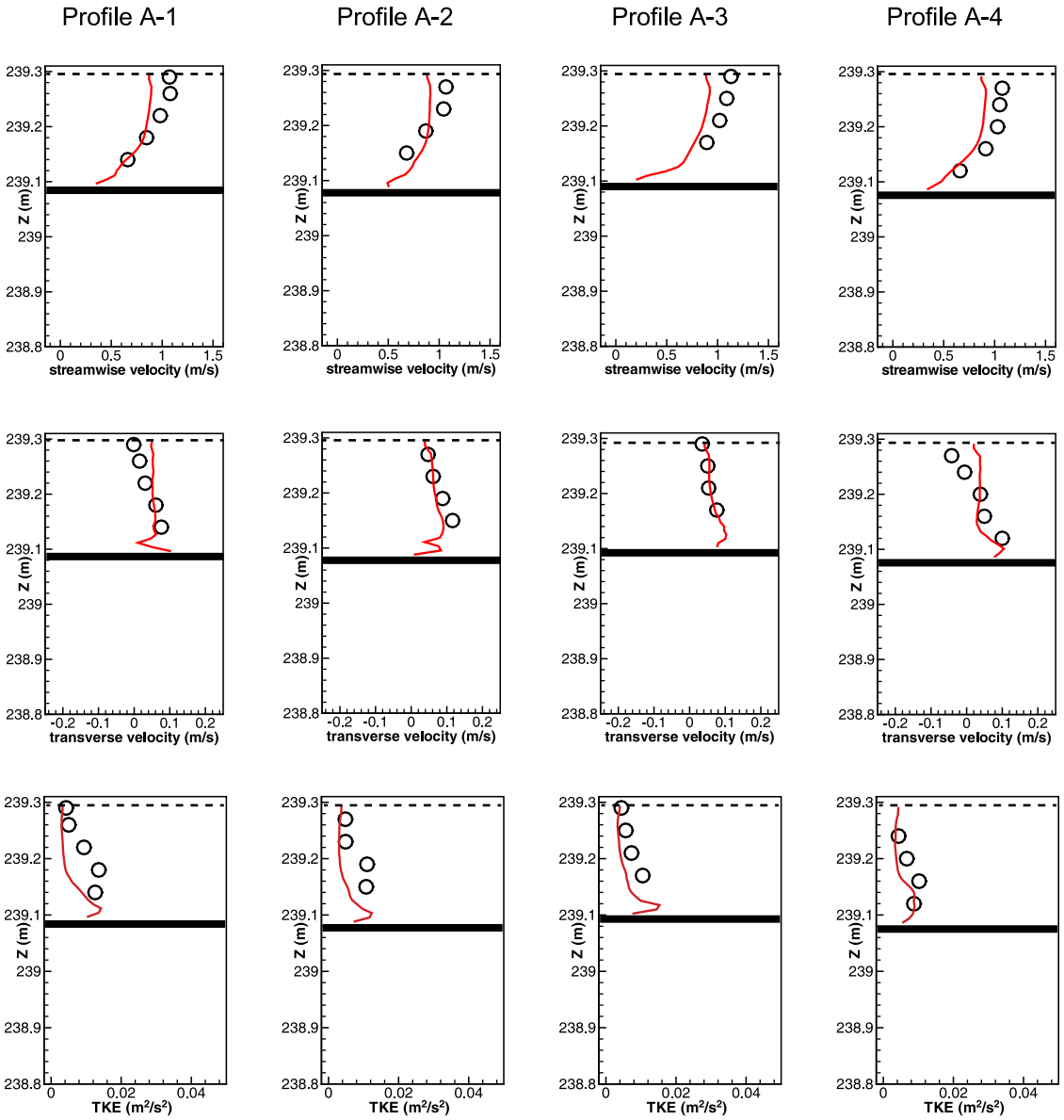

Figure 6. Comparisons of mean streamwise velocity, mean transverse velocity, and TKE with the measurements at the cross section A (solid line, LES; symbols, measurements). The locations of the cross section and each profile within a cross section are defined in Figure 3. The dashed line and thick solid line denote the locations of free surface and bed, respectively.

condition at the immersed boundary nodes. The roughness effect of the fine sand with grain size less than 1 mm in the pool is neglected, i.e., the bed in the pool was assumed to be smooth and the effect of sand grain roughness was neglected. However, large roughness elements in the riffle region with size in the range of 10 cm to 15 cm are directly resolved by using horizontal grid spacing of 1.5–2.0 cm. At the outlet, the zero gradient velocity boundary conditions are employed.

[19] The computational time step was chosen as 0.002 s, which corresponds to CFL (Courant-Friedrichs-Lewy) number of 0.6, and the computation was carried out by using 120 CPUs on a supercomputer. The simulation was first run until the total kinetic energy in the computational domain reached steady state. The simulation was continued for 10^5 time steps, which corresponds to about 6.5 flow through times for a 30 m long computational domain, and the data collected during this simulation interval were averaged to calculate the mean flow and turbulence statistics.

4. Numerical Model Validation

[20] The LES flow solver has already been validated by *Kang et al.* [2011] who carried out simulations for flow in the OSL at base flow condition. The Reynolds number (Re), Froude number (Fr), and flow rate (Q) of the base flow condition were $Re = 2.4 \times 10^4$, $Fr = 0.3$, and $Q = 4.4 \times 10^{-2}$ m^3/s, respectively, where Re and Fr are based on the flow depth and bulk velocity at the inlet. The simulated mean velocity field and TKE profiles at several locations within

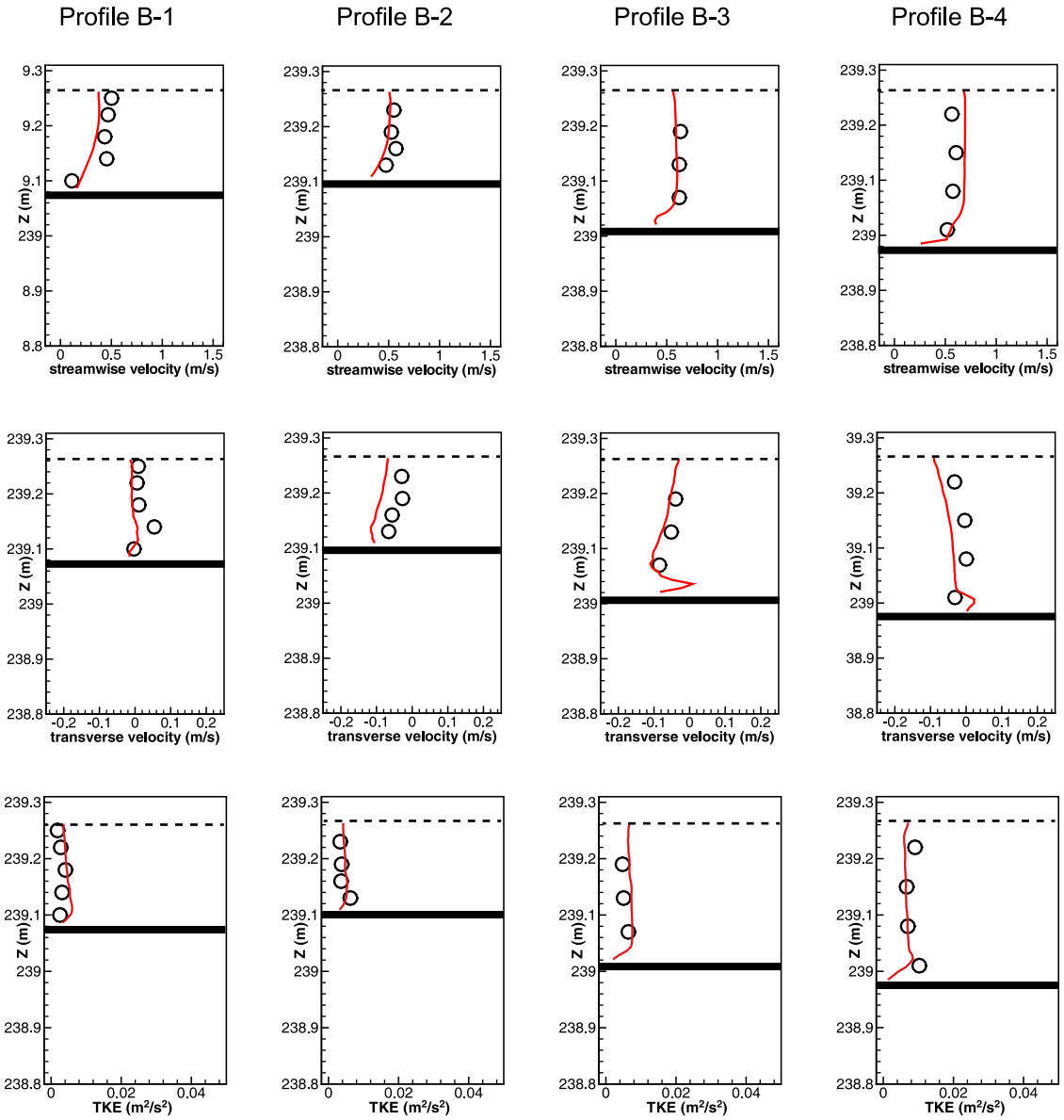

Figure 7. Comparisons of mean streamwise velocity, mean transverse velocity, and TKE with the measurements at the cross section B (solid line, LES; symbols, measurements). The locations of the cross section and each profile within a cross section are defined in Figure 3. The dashed line and thick solid line denote the locations of free surface and bed, respectively.

the meander bend were found to be in good overall agreement with the measurements. In this section we provide additional validation of our model for flow in the OSL at bankfull conditions, which yields a much higher Reynolds number ($Re = 10^5$) than the previously reported base flow condition reported by *Kang et al.* [2011] ($Re = 2.4 \times 10^4$).

[21] Velocity measurements were carried out at 7–9 profiles with 4–6 vertical measurement points at four cross sections. Figure 3 shows the locations of those four profiles at each cross section. Two cross sections (A and D) were placed near the downstream end of the first and second riffles, respectively, while the other two measurement cross section (B and C) were located within the meander bend. As shown in Figure 3, the profile locations are numbered from the inner bank to the outer bank.

[22] Figures 6–9 compare the computed mean velocity and TKE profiles with the measurements at cross sections A, B, C and D, respectively. Total number of measurement points at the four cross sections are 116, but only four profiles at each cross section are compared with the computed results in Figures 6–9. The first and second letters of the captions in Figures 6–9 denote locations of the cross section and the profile, respectively. It is seen that the simulations are in good overall agreement with the measurements. Notice in particular that the computed transverse velocity component is predicted reasonably well, both in terms of its sign and magnitude, which points to the conclusion that the LES captures the magnitude of the secondary motion within the bend with good accuracy. However, some discrepancy between the measurement and

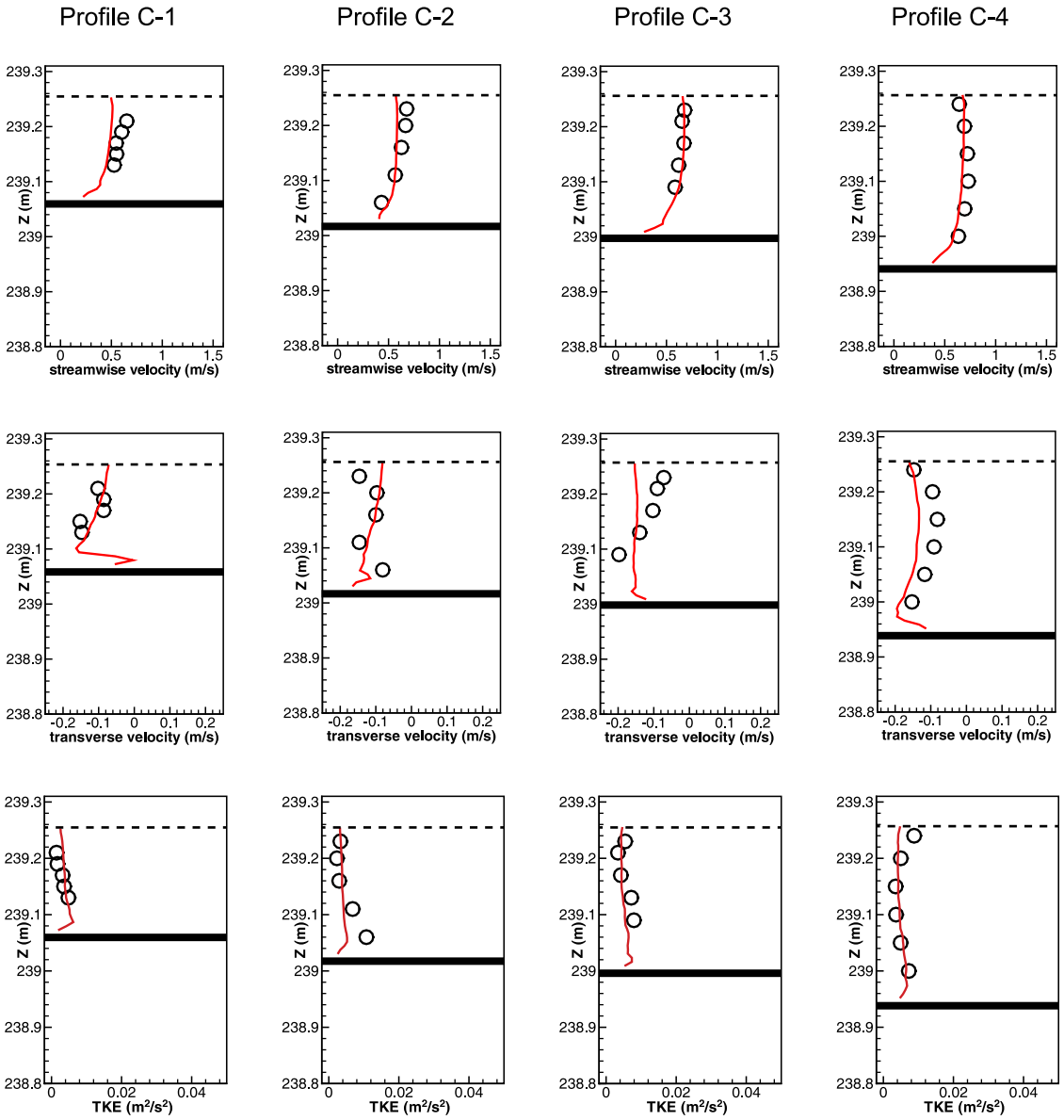

Figure 8. Comparisons of mean streamwise velocity, mean transverse velocity, and TKE with the measurements at the cross section C (solid line, LES; symbols, measurements). The locations of the cross section and each profile within a cross section are defined in Figure 3. The dashed line and thick solid line denote the locations of free surface and bed, respectively.

simulation are also observed. For instance, the transverse velocities at C-3 and D-2 are not predicted very well.

[23] It is also worth noting that the overall level of agreement between the simulations and the experiments improves somewhat from cross section B and beyond. Recall that the inflow conditions prescribed at the start of the computational domain were obtained from a separate LES of fully developed flow in a straight channel with cross section that of the inlet cross section. Such inflow conditions are unlikely to accurately represent the state of the actual flow at the inlet, which enters the channel from the headbox flow control structure as shown in Figure 1. The overall good agreement between measurements and experiments, especially downstream of the first riffle, points to the conclusion that the riffle acts to homogenize the flow, causing it to accelerate and increasing significantly turbulent mixing (see below), thus, minimizing upstream memory effects. This is an important finding of this work since prescribing inflow conditions in numerical simulations of natural streams is not only challenging for the OSL but for any field case as well. This issue will be discussed in more detail in section 5.1.1 of this paper.

[24] The overall level of agreement between experiments and simulations emerging from Figures 6–9 is particularly encouraging when one considers the uncertainties inherent in our numerical model and the fact that no attempt was made to calibrate the model in any way. These uncertainties include (1) the dynamic bed morphologic condition and the fact that it was not possible to scan the entire bed simultaneously as discussed above; (2) the aforementioned uncertainties in the

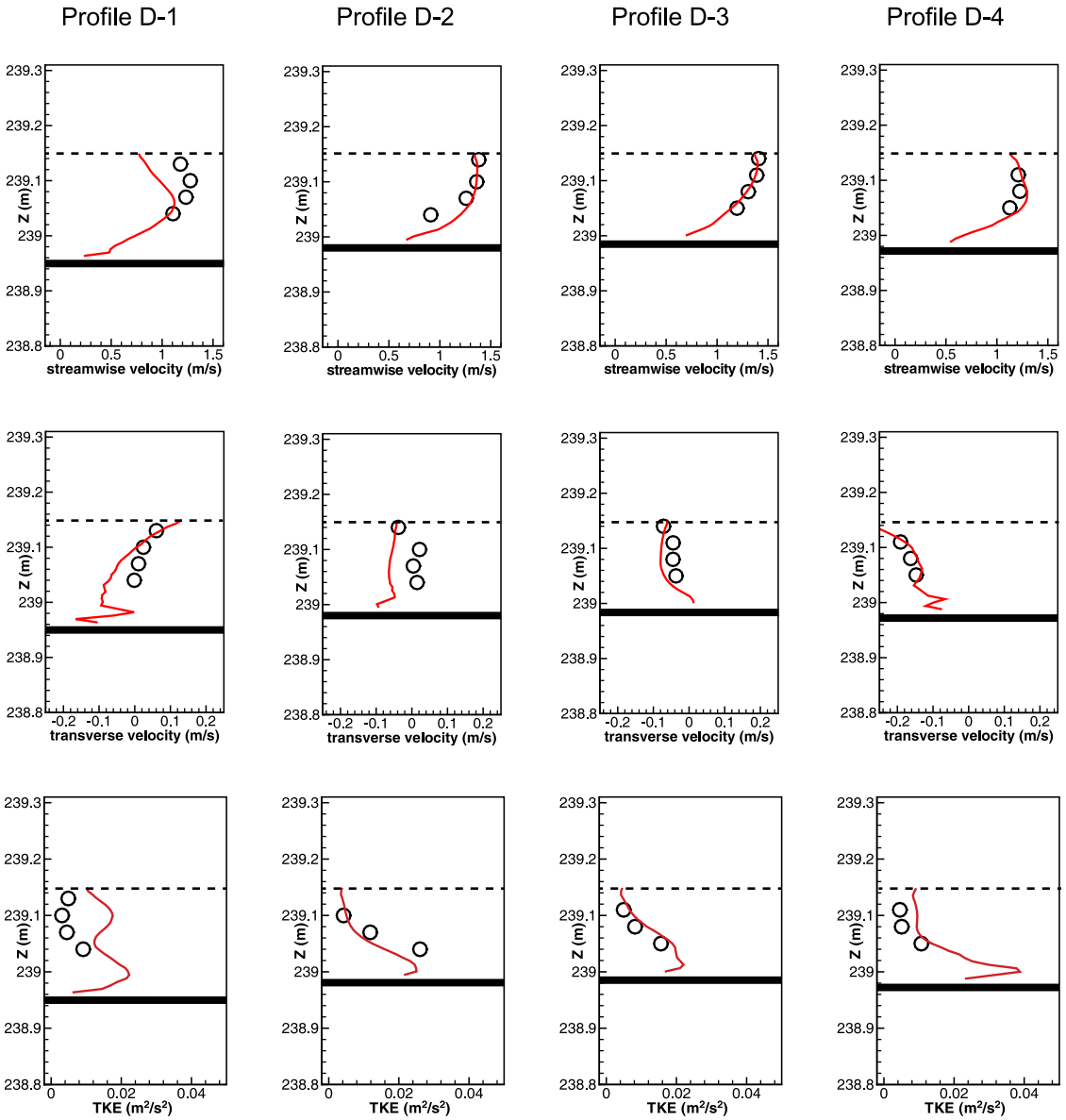

Figure 9. Comparisons of mean streamwise velocity, mean transverse velocity, and TKE with the measurements at the cross section D (solid line, LES; symbols, measurements). The locations of the cross section and each profile within a cross section are defined in Figure 3. The dashed line and thick solid line denote the locations of free surface and bed, respectively.

inflow boundary conditions, which are likely to impact, at least to some degree, the accuracy of the flow in the vicinity for the first riffle; (3) the possible influence of the sand roughness in the pool zone, which was not taken into account; and (4) the effect of vegetation planted on the stream bank on the flow, which is neglected in our simulation. It is also possible that the above mentioned uncertainties contributed to the small discrepancies between computations and measurements shown in Figures 6–9.

[25] To better quantify the level of agreement between experiments and simulations, we show in Figure 10 the scatterplots of computed versus measured flow variables at all 116 velocity measurement points including those not shown in Figures 6–9. Slopes, intercepts and squared correlation coefficients (r^2) obtained from linear regression are also presented. In Figure 10, C and M denote the computed and measured values, respectively. The values of the obtained squared correlation coefficients and slopes for the mean streamwise and transverse velocity show strong agreement between computation and measurement. Taking into account the previously mentioned uncertainties in the field experiment, such level of agreement is very promising and demonstrates the accuracy of the numerical model. The TKE shows weaker overall correlation than the mean velocities. Figure 10c shows a nonzero intercept and a random discrepancy between measured and predicted TKE, rather than a consistent bias. This suggests possible error in the model results as well as in the ADV measurements. The error in the measurement can be due to the inherent limitations of the ADV and in particular the well-known issue

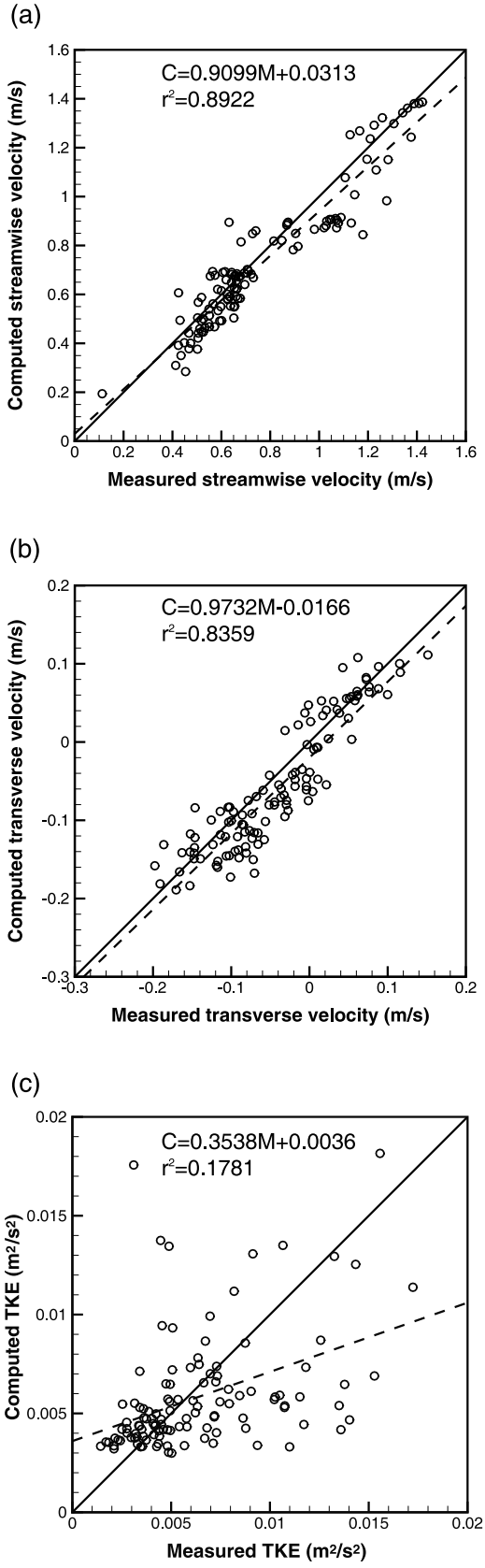

Figure 10. Scatterplots of computed and measured (a) mean streamwise velocity, (b) mean transverse velocity, and (c) TKE at all 116 ADV points where measurements were obtained. Solid and dashed lines show the perfect fit and linear regressions using least squares fits, respectively. C and M and denote the computed and measured values, respectively, and r^2 is the squared correlation coefficient.

of Doppler noise, which is known to affect the accuracy of the measured TKE measurements [*Lohrmann et al.*, 1994; *Nikora and Goring*, 1998]. The error in the computational model can be attributed to relatively coarse grid resolution (140–400 wall units). It is also possible that neglecting the sand grain roughness in the computation partly accounts for the underestimation of the TKE.

[26] Finally, to quantify the range of scales of motion resolved by the LES we plot in Figure 11 the one-dimensional power spectral density (PSD) of the computed and measured streamwise velocity fluctuations at two representative locations in the riffle and pool zones. The two measurement points in the pool and riffle are positioned approximately 7 cm below the water surface in the pool and the second riffle, respectively. The regions with −1 and −5/3 slopes indicate the production range and inertial subrange, respectively, and the regions with a steep slope at high frequencies show the dissipation range. The production range represents the production of turbulence energy by low frequency coherent structures while the inertial subrange marks the cascade of the energy from the larger to smaller eddies. Finally, the dissipation range indicates the dissipation of energy occurring at the subgrid level due to molecular and SGS model viscosities. A dissipation range is not observed in the measured spectra, which implies that the dissipation range is located at frequencies higher than 25 Hz. The observed relatively sudden, nonphysical drop in the computed PSD at frequencies of 5–10 Hz indicates the flow scales smaller than those frequencies are not resolved by the LES. This should be attributed to the combined effect of insufficient grid resolution and the effect of the SGS model At both locations shown in Figure 11, the overall agreement between the measured and computed power spectral density is satisfactory.

[27] It is important to point out that the cutoff frequency in LES is determined by the local mean velocity and the size of the filter of the LES model and not by the computational time step Δt. Therefore, using $\Delta t = 0.002$ s does not mean that the LES can resolve up to the frequency of 500 Hz. Using Taylor's hypothesis, the cutoff frequency at each grid cell can be approximately calculated by $f = U_\Delta/\Delta$ and $f_N = f/2$, where U_Δ and Δ are the magnitude of mean velocity and the size of the filter, respectively, and f_N is the Nyquist cutoff frequency. By assuming $U_\Delta = 0.5$ m/s and $\Delta = 0.02$ m, one obtains $f_N = 12.5$ Hz, which is slightly higher than the frequencies at which the computed spectra suddenly drops (5–10 Hz).

5. Discussion of Flow Physics

5.1. Instantaneous and Mean Flow Patterns at 2-D Planes

[28] In this section we start the discussion of the simulated flow physics by presenting visualizations of the instanta-

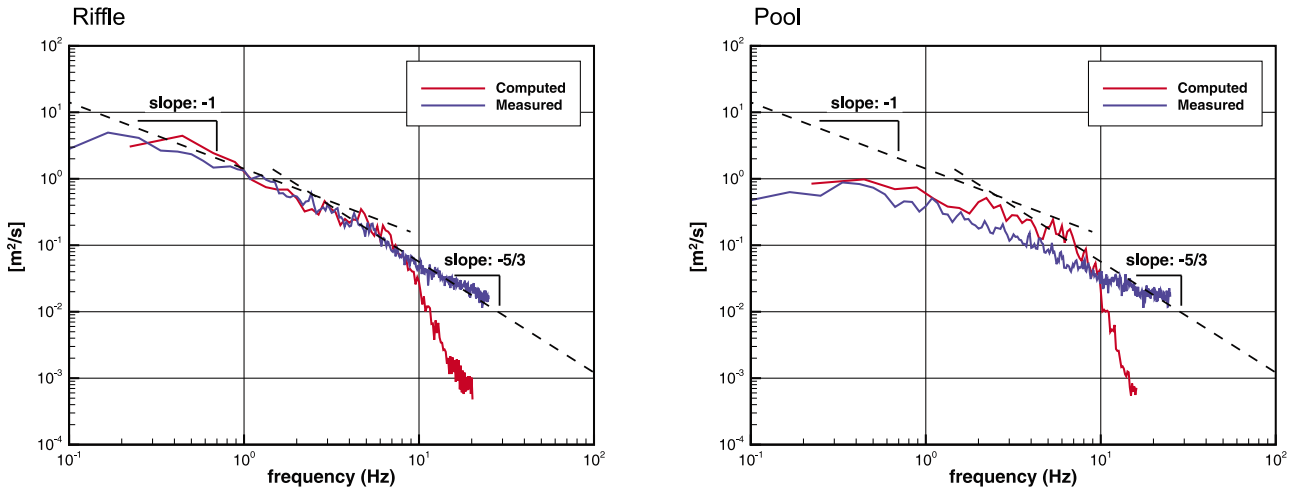

Figure 11. Power spectral density of computed and measured streamwise velocity fluctuations at representative locations in the riffle and pool zones.

neous and time-averaged flowfields at two two-dimensional planes: (1) the water surface and (2) the near-bed plane located 18 cm below the water surface. Figures 12, 13, and 14 show contours of the instantaneous streamwise velocity component, mean streamwise velocity component, and TKE, respectively, at these two planes. We begin our discussion by considering the flow patterns in the riffle followed by flow phenomena in the pool region.

5.1.1. Flow Patterns in the Riffle

[29] To better illustrate the structure of the near-bed flow in the riffle, we zoom in Figure 15 in the second riffle region plotting instantaneous velocity magnitude, TKE and Reynolds shear stress contours at a near-bed plane, which is located 18 cm below the water surface. Figure 15 clearly illustrates the ability of our method to resolve the dynamics of vortex shedding from discrete roughness elements on the bed. As seen in Figure 15, for instance, small rocks of varying size and other bed features protrude above the visualization plane and unsteady wake structures are shed from each one of these complex bed features. These wakes interact with each other and the streambed giving rise to a highly dynamic and very rich flow environment near the bed.

[30] The intensity of the flow unsteadiness in this region is evident in Figure 15, which highlights the ability of the near-bed energetic coherent structures to produce high levels of TKE and Reynolds shear stresses. It is worth noting that pockets of high TKE occur both upstream and downstream of individual roughness elements, which should be attributed to the complex web of vortical structures induced by the various bed features. The resulting instantaneous flow environment is very complex, highly dynamic and is characterized by intense turbulent mixing. Another important feature of the near-bed riffle flow that is evident in Figure 15, is the intense interaction among the wakes shed from each roughness element. As observed in Figure 15, such interactions raise the TKE and Reynolds shear stress levels significantly in between the various bed features causing high overall levels of turbulent mixing throughout the riffle region.

[31] An important consequence of increased turbulent mixing and high Reynolds stresses near the bed is that fine sediments can not be deposited inside the riffle. Only coarser rocks, which can withstand high shear stress, can thus remain in the riffle, thus, pointing to the hydrodynamic reasons for the so-called bed armoring process [*Vanoni*, 1975]. This point will be discussed further in section 5.4

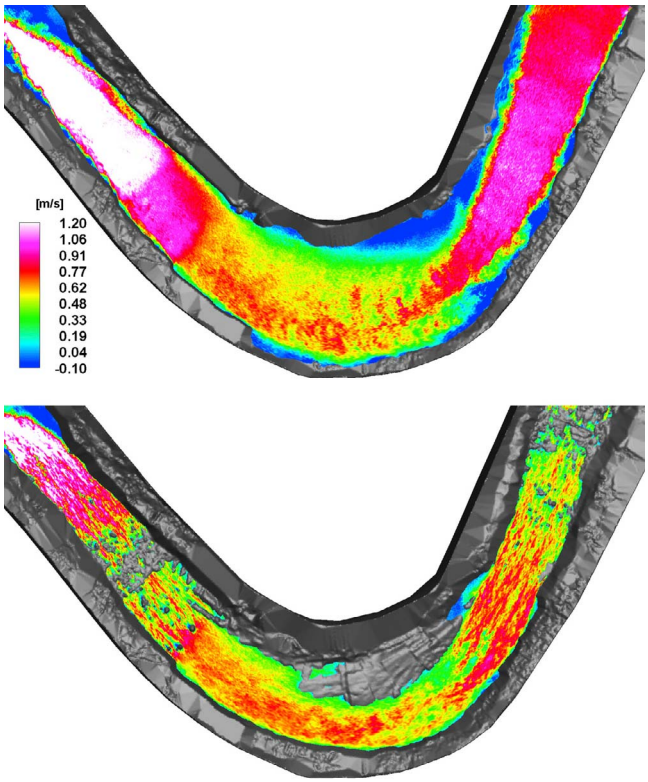

Figure 12. Instantaneous streamwise velocity contours (top) at the water surface and (bottom) at the near-bed plane (flow is from right to left).

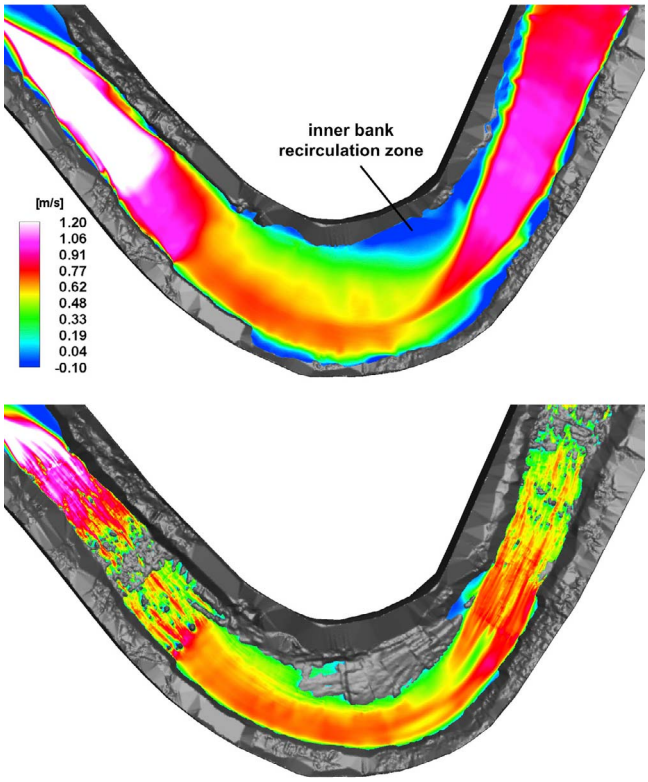

Figure 13. Mean streamwise velocity contours (top) at the water surface and (bottom) at the near-bed plane (flow is from right to left).

where we discuss the wall shear stress patterns at the streambed.

[32] As already mentioned in section 3.2, the inlet conditions for this simulation were extracted from a separate LES of fully developed turbulent flow in a straight reach with the same cross section as the inlet cross section of the computational domain. Such inflow conditions do not reproduce the first- and second-order statistics of the measured velocity at the inlet correctly and could thus influence the accuracy of the simulated flowfields in the meander bend. As we showed in section 4, however, the computed mean velocities in the riffles and the pool agree well with the measured data, which already led us to speculate that the flowfield downstream of the riffle is not much affected by errors due to incorrect inlet boundary conditions. The results we have presented in this section clearly show that the complex and very dynamic instantaneous flow environment induced by roughness elements in the riffle renders the flow well mixed and developed within a short distance, thus, diminishing "memories" of upstream flow conditions. The reason that riffle roughness in this case appears to be very effective in this regard should be attributed to the shallowness of the flow, which yields values of the roughness-height-to-channel-depth ratio to be as 50 percent of the flow depth in the riffle. Consequently, the effects of bed roughness are felt throughout the water column causing intense turbulent motions that destroy upstream originating coherent structures and produce an essentially brand new flowfield that is nearly independent of upstream conditions. Obviously, for deeper flows, such as those that can occur during a flood, riffles may not be as effective as in the present case in homogenizing the flow. Therefore, numerical simulation of such cases may well require more careful specification of upstream boundary conditions especially if the flow details within the first meander bend are of interest.

5.1.2. Flow Patterns in the Pool

[33] We next investigate the simulated flow patterns in the pool. Figures 12 and 13 show that as the high-momentum flow from the first riffle enters the pool it narrows forming a strong jet-like flow structure at the water surface. This jet is seen to approach the outer bank of the bend, reaching the apex where the thin high-velocity core breaks down and starts diffusing laterally to cover a larger area of the outer bank before it encounters the second riffle. As further seen in Figure 13, the high-velocity jet appears to become wider in the near-bed plane and is positioned above the thalweg of the bend. The emergence of such high-velocity core near the bed along the outer bank and the thalweg is expected to accelerate stream bank and streambed erosion as is known to occur in meander bend flows [*Frothingham and Rhoads*, 2003; *Blanckaert*, 2009, 2010; *Jamieson et al.*, 2010].

[34] Another important feature of the surface flow that is evident from Figures 12 and 13 is that the narrowing of the high-velocity core from the riffle and the formation of the jet-like flow appears, at least at first glance, to be linked to the lateral constriction of the surface flow due to the pockets of negative streamwise velocity that form along both the

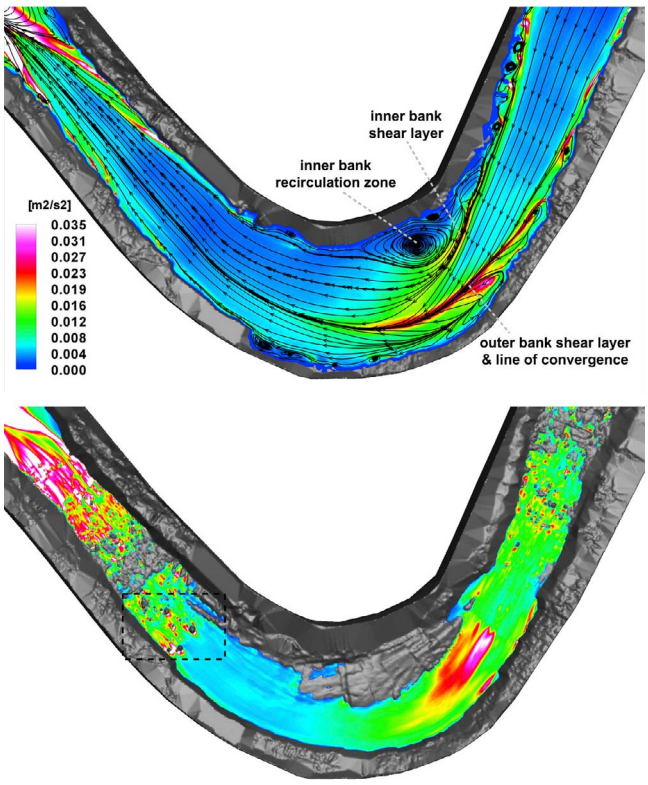

Figure 14. (top) TKE contours and mean limiting streamlines at the water surface and (bottom) TKE contours at the near-bed plane (flow is from right to left). The dashed-line rectangle indicates the domain shown in Figure 15.

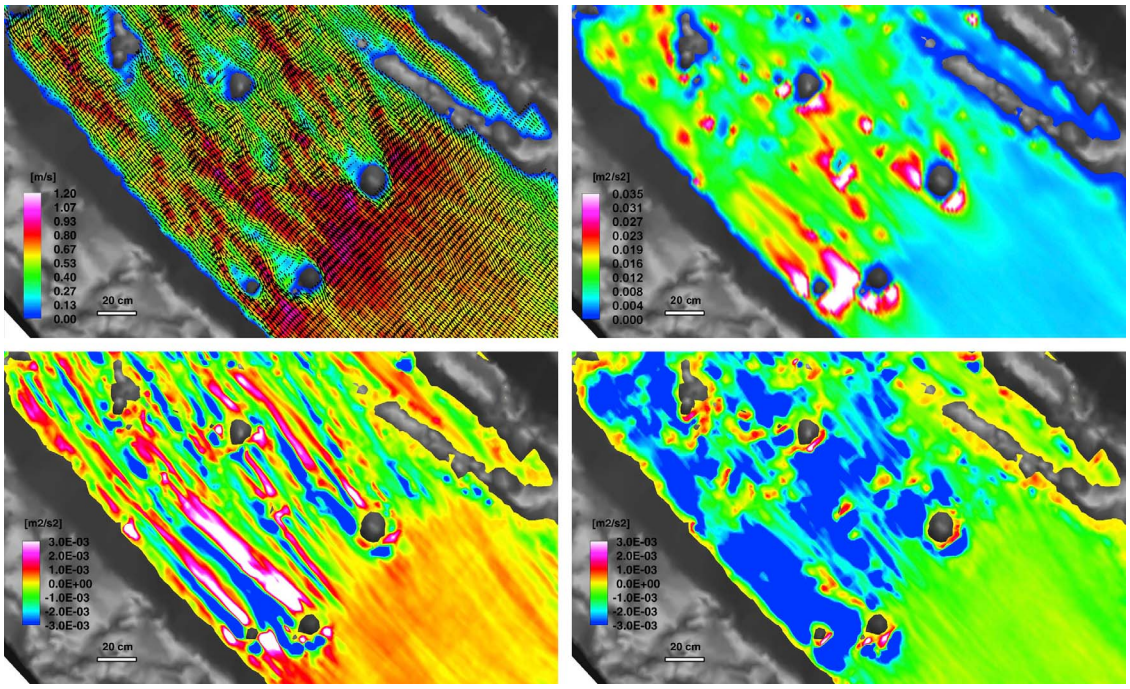

Figure 15. (top left) Computed instantaneous 2-D velocity vectors and velocity magnitude contours, (top right) TKE contours, (bottom left) $\overline{U'V'}$ contours, and (bottom right) $\overline{U'W'}$ contours at the near-bed plane of the second riffle region (flow is from bottom right to top left; U', V', and W' denote the velocity fluctuations in the streamwise, transverse, and vertical directions, respectively). Every two grid points in the streamwise direction are shown in the 2-D vector plot (Figure 15, top left). See Figure 14 for the location of domain.

inner and outer banks of the pool. These are regions of slow recirculating flow with the inner bank recirculation zone being the largest and most prominent feature; this important feature of the flow will be discussed in more detail in section 5.3 (see Figures 14 and 21 and section 5.3). Juxtaposing the instantaneous and mean streamwise velocity contour plots in Figures 12 and 13 clearly show that the high-velocity jet entering the pool, the region of increased streamwise velocity along the outer bank and the pockets of recirculating flow along the inner and outer banks are all rather stable, large-scale features of the flow that are present at all times.

[35] The intensity and spatial extent of flow unsteadiness due to the aforementioned complex flow features in the pool is quantified in Figure 14, which depicts contours of TKE at the water surface and near-bed plane. Figure 14 also includes mean streamlines at the water surface to facilitate subsequent discussion concerning the links between mean flow patterns and TKE production. There are two distinct thin layers of increased TKE at the water surface that emanate from the inner and outer banks of the bend and mark the outer edges of the previously discussed high-velocity jet (see Figure 14). We shall refer to these two pockets of increased TKE as the inner and outer bank shear layers, respectively. The inner bank shear layer is seen to delineate exactly the slow moving flow in the inner bank recirculation zone from the fast traveling outer flow. The reason for the formation of such a shear layer and the associated pocket of increased TKE is easily understood since it is well known that flow separation creates a free shear layer along the boundary of the recirculation zone leaving a clear footprint of high levels of TKE [*Le et al.*, 1997]. While the levels of TKE within the inner bank shear layer decay rather quickly at the downstream end of the inner bank recirculation zone, the pocket of increased TKE marking the outer bank shear layer intensifies and stretches to reach up to the apex of the bend. This is a rather striking and perplexing feature of the flow, which, unlike the inner bank shear layer, cannot be readily explained by the presence of the small pockets of reversed flow along the outer bank of the bend. In fact, and as clearly revealed by the mean surface streamlines superimposed in Figure 14, the outer bank shear layer is seen to coincide exactly with a line of convergence in the mean streamlines along which water surface flow from the outer bank is seen to collide with flow originating near the inner bank. Such line of convergence is the clear mark of three-dimensional separation [*Tobak and Peake*, 1982] at the water surface in the sense that it must be accompanied by a downward flow from the surface toward the bed. Clearly, therefore, the mechanism that gives rise to the outer bank shear layer is fundamentally different than that generating its inner bank counterpart. As we will subsequently show in section 5.2, this mechanism is linked to the three-dimensional redistribution of streamwise momentum within the pool induced by the complex secondary flow patterns that develop within the bend.

[36] Finally, comparing the TKE contours at and below the water surface in Figure 14, underscores the three-dimensionality of the flow within the pool. As seen Figure 14, for instance, the inner and outer bank shear layers

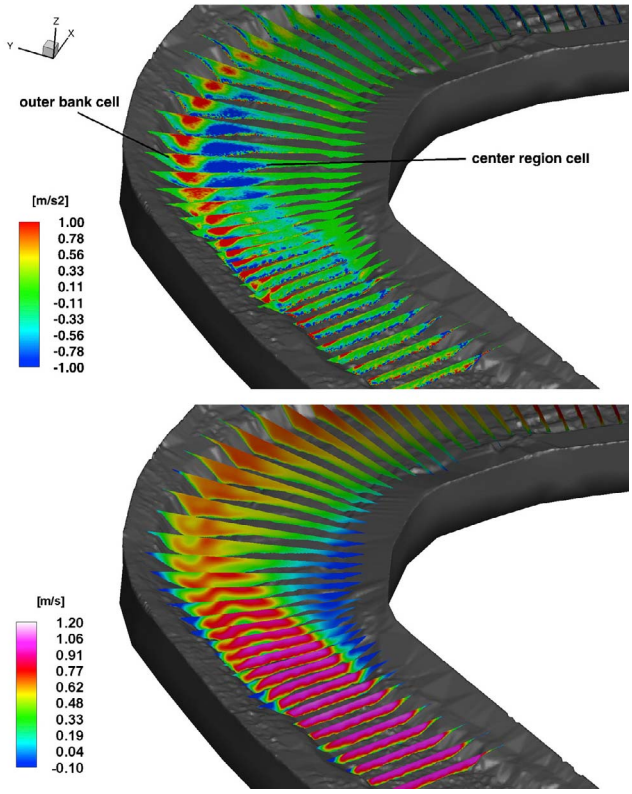

Figure 16. Three-dimensional visualization of the simulated mean flow patterns by contour plots of (top) mean helicity and (bottom) streamwise velocity in a series of cross sections through the channel (flow is from bottom to top).

that are present at the water surface are not evident at the near-bed plane. Instead a pocket of high TKE is seen to originate at the interface between the shallow riffle and the deep scour pool. This pocket marks the laterally oriented recirculating eddy created by the sudden, step-like change of bed elevation that generates a shear layer above the deep scour pool.

5.2. Secondary Flow Patterns

[37] To visualize helical secondary flow within the channel we employ the helicity (or helicity density) proposed by *Moffatt* [1969], which is a scalar quantity defined as follows:

$$H = \vec{u} \cdot \vec{\omega}, \tag{6}$$

where $\vec{u}$ and $\vec{\omega}$ ($= \nabla \times \vec{u}$) are the velocity and vorticity vector, respectively. By definition, the helicity H becomes large in regions where the velocity and vorticity vectors are aligned and as such this quantity can be used to identify streamwise vortices in the flow without depending on local of the vortical structure. cross section and coordinate system definitions. Moreover, the sign of H readily indicates the sense of rotation We employ helicity instead of streamwise vorticity for visualizing the secondary motion because in a channel with varying radius of curvature the direction of the longitudinal grid lines may not always coincide with the streamwise flow direction, which furthermore is difficult to define in a natural stream. The helicity, however, is a more objective and straightforward to calculate in natural streams metric for visualizing streamwise vortices as it is a scalar quantity independent of the orientation of the cross section.

[38] In Figure 16 we plot side by side contours of the mean helicity and streamwise velocity, respectively, at several cross sections within the channel. When looking downstream, positive and negative values of helicity imply clockwise and counterclockwise streamwise helical motions, respectively. Figure 16 reveals a range of complex three-dimensional flow phenomena at various regions within the channel. First, in the straight and shallow riffle zone the helicity contours suggest the presence of multiple streamwise vortical structures along the bed, which distort the isovels both along the bed and near the banks. This finding is similar to the observation of *Blanckaert et al.* [2010] who investigated experimentally secondary flow patterns in a trapezoidal open channel. The presence of streamwise streaks of helical secondary motion in this region is the result of the anisotropy of the Reynolds stresses induced by the combined effects of the channel walls, the water surface and the heterogeneous roughness distribution along the streambed [*Naot*, 1984; *Tominaga et al.*, 1989].

[39] Downstream of the riffle, the helicity contours reveal that the secondary flow structure transitions from multiple streamwise streaks to a more organized two-cell structure marked by the regions of negative and positive helicity along the central part and outer bank of the bend, respectively (see Figure 16). These are well known from previous studies on center region and outer bank cells, denoted hereafter as CRC and OBC, respectively [*Hey and Thorne*, 1975; *Bathurst et al.*, 1979; *Thorne et al.*, 1985; *Blanckaert and de Vriend*, 2004; *van Balen et al.*, 2009]. When looking downstream the CRC rotates in the counterclockwise direction (negative helicity), such that near-bed flow moves toward the inner bank, and is located closer to the channel bed toward the inner bank. This cell originates via the classical secondary flow mechanism in meander bends and is driven by the imbalance between centrifugal force and transverse pressure gradient [*Van Bendegom*, 1947; *Rozovskii*, 1957; *Engelund*, 1974; *de Vriend*, 1977; *Humphrey et al.*, 1981; *Johannesson and Parker*, 1989]. Both the intensity and size of the CRC are seen to increase rapidly as the flow encounters the point bar, presumably due to the local increase in streamwise curvature induced by the presence of the point bar, and appear to be maximized at the apex of the bend. Downstream of the apex, however, the CRC starts decaying and its strength weakens considerably upstream of the second riffle. The OBC, on the other hand, is attached to the water surface and persists well beyond the apex of the bend even after the CRC has decayed fully. A striking finding from Figure 16 (also see Figure 17), which differs from what has been found in idealized laboratory bends, is that the OBC can be stronger than the CRC downstream of the apex. This implies that the flow structure in a natural meander bend with complex bed topography can be different from that in an idealized bend, but it is also possible that such a conclusion is related to the geometric characteristics of the specific configuration we study herein. One may also raise the question that the longer persistence of the OBC shown in Figure 16 is due to the larger velocity magnitude along the outer part of the bend than that in the center region, which contributes to the local increase of the helicity magnitude. To investigate this issue we

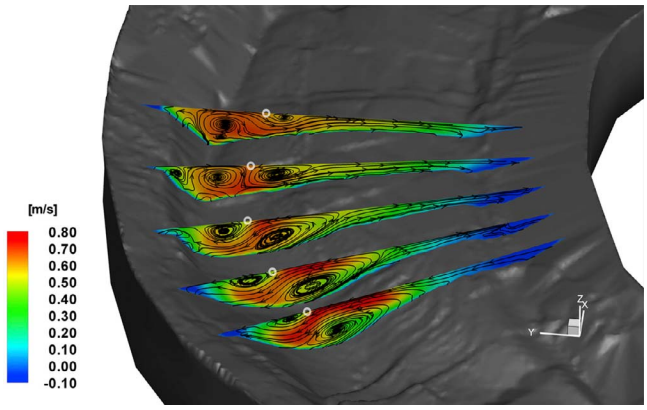

Figure 17. Contours of mean streamwise velocity and two-dimensional streamlines at cross sections near the apex (circles denote half saddle points; flow is from bottom to top).

have also examined the streamwise vorticity field calculated by assuming that the streamwise flow direction coincides with the longitudinal grid lines and found the same trend regarding the downstream persistence of the OBC as that revealed by the helicity plot in Figure 16. Ultimately, both cells are seen to decay well upstream of the second riffle. This finding is consistent with the field observation of *Frothingham and Rhoads* [2003] who observed that helical motions disintegrate as the flow moves out of the bend, thus, implying that each pool-riffle sequence involves its own physical processes of generation and destruction of helical motions, which are decoupled by those of previous sequences. However, it was also reported [see, e.g., *Abad and Garcia*, 2009] that in successive meander bends secondary flow produced in the previous bend could influence the secondary flow patterns in the next bend. This indicates that it is possible that specific geometric characteristics of the meander planform can affect the disintegration of the upstream helical motion and its interaction with downstream helical flow patterns.

[40] The overall structure and relative location of the OBC in our simulations is in good agreement with previous laboratory and numerical findings with curved open channels of prismatic cross section [*Blanckaert and de Vriend*, 2004; *van Balen et al.*, 2009; *Stoesser et al.*, 2010] as well as consistent with previous field observation [*Hey and Thorne*, 1975; *Bathurst et al.*, 1979; *Thorne et al.*, 1985].

[41] The existence of the two secondary cells has a profound effect on the redistribution of mean streamwise momentum within the bend as seen in Figure 16. The fairly uniform in the lateral direction high mean streamwise momentum core that occupies almost the entire cross section at the end of the riffle gets distorted near the outer bank as it enters the bend, plunging sharply toward the streambed and giving rise to a region of reduced streamwise velocity near the water surface along the outer bank that extends up to the apex of the bend. To further elucidate the highly three-dimensional structure of the flow in this region, we plot in Figure 17 contours of the streamwise velocity superimposed with two-dimensional streamlines at few cross sections near the apex. In addition to the clear depiction of the manner via which the CRC and OBC redistribute mean streamwise momentum within the cross section, Figure 17 also clarifies the downstream evolution and interaction of the two cells. The size of the CRC is much larger than that of the OBC at the first cross section in Figure 17. At the second and third cross sections, the CRC still dominates the cross-sectional flowfield but the OBC starts growing in size. At the fourth cross section, the OBC grows further and its size is now comparable to that of the CRC while an additional very small cell rotating in the counterclockwise direction is observed near the corner of the outer bank. At the last cross section in Figure 17, which is located near the apex of the bend, the CRC has nearly disappeared while the OBC is still present. From the well mixed streamwise velocity contours at this last section, however, it is evident that the intensity of both cells has diminished a great deal, and as a result they are no longer capable of redistributing mean streamwise momentum.

[42] Figure 17 also reveals that a key feature of the surface flow near the outer bank in the vicinity of the apex of the bend is the presence of a half saddle point in the secondary flow streamlines, marked by a circle. Using terminology from topological fluid mechanics [*Tobak and Peake*, 1982], the stable manifolds of this saddle are defined by the inward directed OBC flow and the outward directed CRC flow along the water surface. Its unstable manifold, on the other hand, is defined by the downward directed common flow between the two secondary flow cells that transports high momentum flow from the water surface toward the streambed. Revisiting now the previously discussed Figure 15, it is evident that the locus of the half saddle points at the cross-sectional streamlines plots is the outer bank line of convergence in the water surface streamlines, which also coincides with the high TKE values defining the outer bank shear layer. As we already mentioned above, this line of convergence is the hallmark of three-dimensional flow separation at the water surface. The cross-sectional streamline plots shown in Figure 17 clearly show that this three-dimensional separation is the result of the collision of the OBC and CRC flows along the line of convergence at the water-surface and the so induced downward common flow along the unstable manifold of the half saddle point at each cross section.

[43] To highlight the structure and intensity of the vertical flow within the bend, we plot in Figure 18 contours of the mean vertical velocity at a plane 12 cm below the water surface. Near the point bar the flow moves upward both at the inner and outer banks, and it converges near the water surface by creating downward flow to the channel bed. As discussed above, converging flow at the water surface is the result of the two colliding counterrotating cells that leads to the formation of the half saddle point at the surface. As seen in Figure 18, the downward flow motion is most intense above the thalweg near the point bar, which suggests that the converging flow at the surface and the so induced strong downward flow are related to the deepening of the channel in support of the field observations of *Hey and Thorne* [1975] and *Thompson* [1986]. As already discussed in section 1, *Hey and Thorne* [1975] observed two secondary cells in natural rivers exhibiting surface flow convergence, which gives rise to channel deepening. *Thompson* [1986] also investigated flow in a meandering gravel bed stream and observed a zone of upwelling adjacent to the outer bank of the stream and inward flow toward a zone of convergence over the deepest part of the pool. The channel deepening at

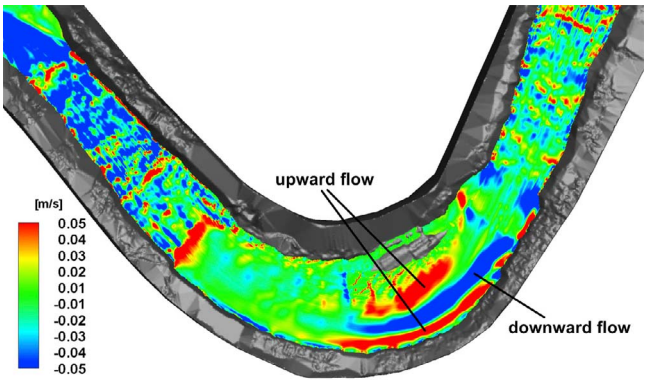

Figure 18. Contours of mean vertical velocity at the plane 12 cm below the water surface (flow is from right to left).

the outer part of the bend is enhanced by the combined effect of the downward flow and the submerged high-velocity core due to momentum redistribution, which increase the local bed shear stress and enhance erosion (see Figure 17). The upward flow motion is intense near the point bar, which points to the conclusion that the CRC, which directs near-bed flow to the inner bank, contributes to the formation of the point bar.

[44] Juxtaposing now Figures 16 and 17 with Figure 14, a clear explanation about the mechanism that gives rise to the previously discussed outer bank shear layer emerges. The collision of the OBC and CRC flows along the water surface at the line of convergence marked in Figure 14 creates a downward directed flow toward the deep part of the pool that transports high momentum fluid from the surface toward the bed. As a result, a low mean streamwise momentum region emerges at the surface near the outer bank and a shear-layer is formed along the line where the two cells collide at the water surface. The mean velocity gradients across the shear layer increase the production of turbulence and give rise to the elongated pocket of high TKE observed in Figure 14 along the outer bank.

[45] To elucidate the mechanisms via which turbulence is produced within the outer bank shear layer (see Figure 14 and section 5.1.2) we plot in Figure 19 contours of the TKE and the three velocity variances at the cross section located at the apex of the bend. At the apex, the x, y and z directions are the streamwise, transverse and vertical directions, respectively. It is evident from Figure 19, that the structure of turbulence in the vicinity of the half saddle point in the cross-sectional streamlines is highly anisotropic. At this point, the lateral velocity variance $\overline{v'v'}$ is much larger than $\overline{u'u'}$ and $\overline{w'w'}$, which shows that essentially all TKE produced in this region is the result of lateral velocity fluctuations at the point where the OBC and CRC flows collide at the water surface. The vertical velocity variance ($\overline{w'w'}$) approaches zero as the water surface is approached because the vertical velocity fluctuations are suppressed by the presence of the water surface. The nearly zero vertical velocity variance ($\overline{w'w'}$) and the high transverse velocity variance ($\overline{v'v'}$) around the half saddle point at the water surface, thus, increase the anisotropy of the transverse and vertical Reynolds stresses ($\overline{v'v'} - \overline{w'w'}$). Since the gradients of this anisotropy term appear in the mean streamwise vorticity transport equation and have been shown to contribute to the production of stress-driven secondary flows in straight channels [*Perkins*, 1970], the results presented in Figure 19 support previous findings that turbulence anisotropy is a major contributing factor in the generation of the OBC in meander bends [*Blanckaert and de Vriend*, 2004; *van Balen et al.*, 2009].

[46] To further investigate the structure of turbulence anisotropy throughout the entire channel, we employ the second invariant of the anisotropy tensor [*Lumley* 1978] defined as follows:

$$II = -\frac{1}{2} b_{ij} b_{ji}, \tag{7}$$

with

$$b_{ij} = \frac{\overline{u_i' u_j'}}{2k} - \frac{1}{3}\delta_{ij}, \tag{8}$$

where u_i' denotes velocity fluctuations in the ith direction, k is the TKE, δ_{ij} is the Kronecker delta, and the overbar denotes the temporal (or Reynolds) averaging. Note that II is a scalar quantity that is invariant to coordinate system transformation and as such it is not sensitive to the specific coordinate system selected to express the velocity field and calculate the components of the Reynolds-stress tensor. In addition, this quantity is identically zero for isotropic turbulence and becomes large in regions where anisotropy becomes important.

[47] Figure 20 shows contours of $-II$ superimposed with secondary flow streamlines at several cross sections through the channel. It is seen that the OBC originates near the entrance of the meander bend in a region at the water surface close to the outer bank where turbulence anisotropy is large. The sense of rotation of the OBC, however, is such that the near-bed flow is directed toward the outer bank. As such, the centrifugal force, which is also directed along the same direction, acts to augment the OBC and sustain it further downstream even in regions where turbulence anisotropy has diminished; see cross sections downstream of the bend apex in Figure 20. When both turbulence anisotropy and curvature effects diminish, however, as the end of the meander bend is approached, the OBC is seen in Figure 20 to decay as well and disappear completely upstream of the second riffle. Therefore, the picture that emerges from our simulations regarding the generation of the OBC in natural meander bends is consistent with that derived from previous experimental and computational studies with open channels of prismatic cross section [*Blanckaert and de Vriend*, 2004; *van Balen et al.*, 2009]. Namely, both turbulence anisotropy effects and the curvature-induced centrifugal force contribute to generate and sustain the OBC in meander bends.

[48] Figure 20 further provides some additional insights into the structure of turbulence in natural meandering streams. First, note that turbulence anisotropy is large overall across the entire cross section throughout the riffle region with pockets of very high anisotropy levels observed near the bed around individual roughness elements. This finding supports our previous discussion that the streamwise vortical structures observed in the helicity plot in Figure 16 within the riffles mark secondary flow cells driven by

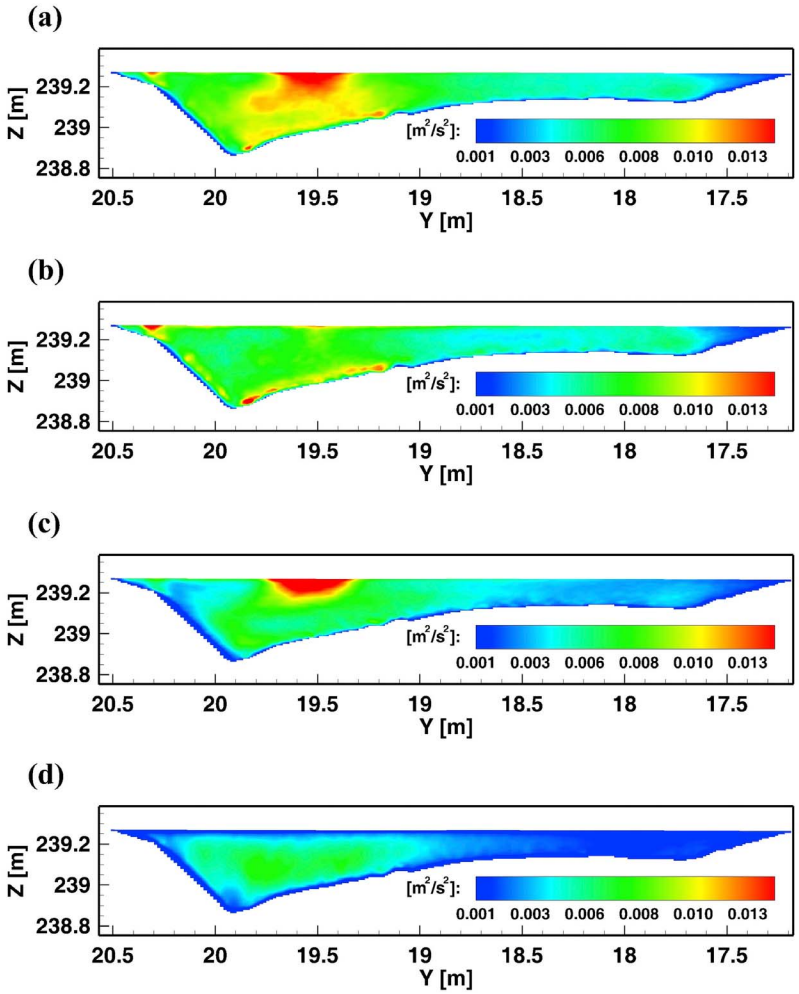

Figure 19. Contour plots of the computed (a) TKE, (b) $\overline{u'u'}$, (c) $\overline{v'v'}$, and (d) $\overline{w'w'}$ at the cross section located at the apex of the bend.

roughness-induced anisotropy. Perhaps the most striking new finding that emerges from Figure 20, however, is that the largest pocket of anisotropy within the channel is observed along the upstream edge of the point bar. This finding is consistent with the fact that the three-dimensional geometry of the point bar increases the complexity of the mean flow causing extra rates of strain, i.e., spatial gradients of all three velocity components along all three spatial directions, that act to enhance the anisotropy of turbulence. Overall, the results presented in Figure 20 show that turbulence anisotropy is important in several regions within natural meandering channels and point to the conclusion that accurate simulation of such flows requires the use of models that can accurately resolve the anisotropy of turbulence.

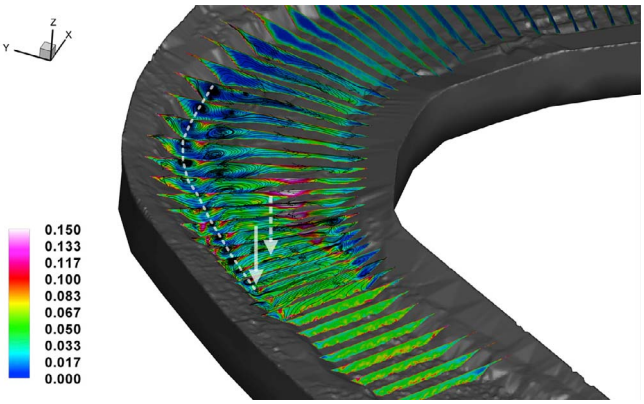

Figure 20. Contours of the $-II$ and secondary flow streamlines in a series of cross sections through the channel. The solid arrow points to the approximate origin of the outer bank cell while the dashed arrow points to the approximate origin of the inner bank cell. The dashed white line traces the approximate streamwise extent of the outer bank cell (flow is from bottom to top).

5.3. Recirculation Zones

[49] The instantaneous and mean velocity contours at the water surface presented in Figures 12 and 13 and streamlines shown in Figure 14 above, revealed the presence of multiple recirculation zones along both the inner and outer banks. To further elucidate the structure of these flow features we plot in Figure 21 three-dimensional streamlines of the mean flow in the vicinity of the point bar superimposed

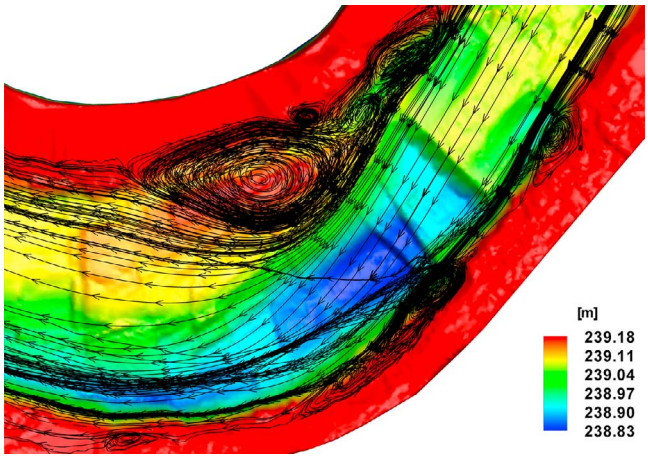

Figure 21. Mean three-dimensional streamlines near the apex of the meander bend superimposed with bed elevation contours (flow is from right to left).

with contour plots of bed elevation. The inner bank recirculation zone is clearly the dominant recirculating flow region in the channel. As seen in Figure 21, the flow in this region consists of a large primary eddy and two smaller, secondary, eddies that collectively span almost the entire point bar. A rather striking feature of the flow that emerges from Figure 21 is that the center of the primary recirculation eddy, where the flow is stagnant in the mean, is located directly above the highest point of the point bar. This finding points to the conclusion that the inner bank flow recirculation plays an important role in the formation of the point bar. It provides a region of reduced velocities (see Figure 13) and low turbulence mixing (see Figure 14 showing very low TKE levels within the inner bank recirculation region) within which fine sediments that are transported there by the CRC flow as bed load could be trapped and deposit. This assertion is consistent with and further supports the works of *Schmidt* [1990] and *Blanckaert* [2010] who observed the formation of sandbars beneath recirculation zones at the water surface.

[50] In addition to the inner bank recirculation zone, Figure 21 also reveals the presence of smaller recirculating flow regions along the outer bank. These appear to be linked to local features in the topography of the outer bank that give rise to pockets of adverse streamwise pressure gradients causing the observed flow separation patterns. As previously discussed, however, these are relatively small scale features of the flow linked to site-specific, local topographic irregularities that do not appear to have a major impact on the overall large-scale flow patterns within the channel. Nevertheless, their presence is important as such topographic variability is certainly present in natural streams and could further enhance the complexity of the flow relative to that obtained in simpler laboratory-scale flumes.

[51] Recirculation or dead zones are important factors in several biogeochemical processes in waterways [*Reynolds*, 2000; *Engelhardt et al.*, 2004]. Such zones are typically characterized by low velocities and can thus increase significantly the residence time of pollutants, nutrients, or suspended sediment loads. It also known that turbulence mixing or velocity can influence the distribution of aquatic organisms such as phytoplankton [*Huisman et al.*, 2002; *Engelhardt et al.*, 2004; *Hondzo and Wüest*, 2009] or fish [*Cotel et al.*, 2006]. Therefore, the low turbulence mixing rate in recirculating regions coupled with the low overall mean flow velocities could significantly impact the quality of aquatic habitats and the ability of streams to support life and process nutrients. The results we presented in this paper show that the arbitrarily complex topography of natural streams could induce several regions of flow recirculation both along the inner and outer banks of the stream.

5.4. Boundary Shear Stress

[52] Boundary shear stress is an important parameter in open-channel flows as it is associated with the potential of streambed erosion and scour and is also used as input to morphodynamic models. It is thus appropriate to conclude our discussion of the flow physics by considering how the previously discussed complex, three-dimensional hydrodynamic environment in the stream impacts the distribution of the boundary shear stress. Figure 22 shows the calculated mean shear stress field along the streambed.

[53] The shear stress distribution in the two riffles is characterized by larger overall magnitudes than in the pool, a trend consistent with the higher overall velocities found in the riffles across the entire water column. It is also evident from Figure 22 that the distribution of the shear stress within the riffle is highly heterogeneous. Multiple small pockets of increased shear stress levels are found that correlate well with the locations of the protruding roughness elements on the bed. The increase of shear stress at these locations should be attributed to the local acceleration of the flow induced by the presence of the roughness elements. Figure 22 further reveals several regions of very low shear stress values throughout the riffle. These regions generally occur in the wake of individual roughness elements, which would tend to be occupied by slower recirculating flow. Overall, however, the regions of very low shear stress in the riffle are considerably fewer than the pockets of very high shear values.

[54] *Keller* [1971] argued that at low flow the mean velocity (or shear stress) in the riffle could exceed that in the pool with the reverse trend occurring during high flows. This is the so-called velocity (or shear stress) reversal phenomenon, which is one of the conceptual models proposed to explain the phenomenon of sediment sorting and the maintenance of pool-riffle sequences in gravel bed streams. In our simulations, however, the overall velocity and boundary shear stress magnitude at the riffles is higher than that in the pool and, therefore, the velocity (or shear stress) reversal proposed by *Keller* [1971] is not observed.

[55] Figure 22 also shows that low shear stress values are observed within the scour pool formed at the pool-riffle transition. The shear stress in this region exhibits a sharp discontinuity from the very high values upstream of the scour pool to nearly zero values in the pool. Such steep gradients can be easily understood in terms of the local bed bathymetry in this region that exhibits a steep, backward facing step-like transition in bed elevation and induces a laterally-oriented recirculation eddy with very low velocities in the scour pool. We note that the discontinuity of the bed topography in these region is purely the result of measurement errors.

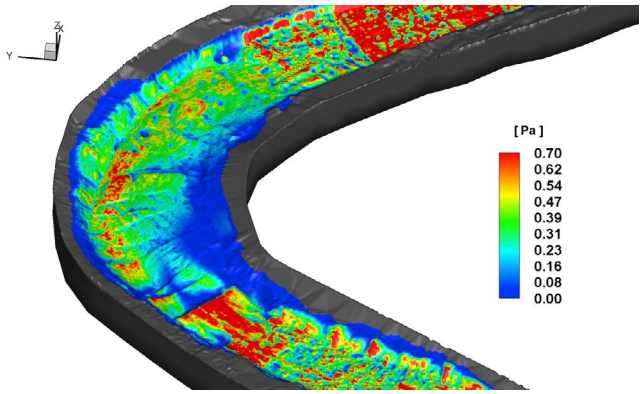

Figure 22. Contours of the mean boundary shear stress (flow is from bottom to top).

[56] Low shear stress values are also found along the inner bank all along the point bar due to the influence of the inner bank recirculation zone that lowers flow velocities. Along the outer bank, on the other hand, the shear stress magnitude is significantly higher with very high values observed along the thalweg of the pool. The mechanism that causes such high shear stress values in the pool has already been discussed above and is linked to the transport of high momentum fluid from the water surface toward the bed by the strong downward flow induced by the combined action of the CRC and OBC in this region. Therefore, Figure 22 in conjunction with our previous discussion in section 5.2 elucidate the impact that the complex and highly three-dimensional interaction between the secondary flow with the streamwise flow through the bend has on the distribution of the boundary shear stress. Such interaction is essentially responsible for increasing the shear stress along the thalweg of the channel, enhancing erosion, and promoting channel deepening.

6. Conclusions

[57] The most important findings of this work are summarized as follows. The flowfield in the riffle is dominated by the heterogeneously distributed, large-scale roughness elements, which (1) increase turbulence anisotropy, (2) give rise to multiple streamwise vortices driven by the anisotropy of the Reynolds stresses, and (3) produce a highly heterogeneous bed shear stress field characterized by multiple pockets of high shear stress intertwined with regions of nearly zero shear stress.

[58] We showed that the OBC originates near the outer bank at the downstream end of the riffle in a region of increased turbulence anisotropy but is sustained well downstream of the apex of the bend even in regions where the anisotropy is negligible. The CRC, on the other hand, appears suddenly as the flow passes around the point bar but decays rapidly at the downstream end of the point bar.

[59] An important finding, which to the best of our knowledge has not yet been reported in previous studies, is that the OBC could persist further downstream than the CRC well after the flow passes the apex. Undoubtedly this finding is the result of the specific geometric configuration we studied herein. Our results, however, lead to the conclusion that meander bend geometries in nature could exist in which the OBC could persist further downstream than the CRC.

[60] The relative location and sense of rotation of the OBC and CRC leads to three-dimensional separation at the water surface along a line of convergence, which marks the collision of the counterrotating OBC and CRC flows and the associated strong downward flow from the surface toward the channel thalweg. Such flow pattern transports high momentum flow from the surface toward the bed reducing the surface velocities near the outer bank and giving rise to the outer bank shear layer while increasing the bed shear stress in the thalweg through the momentum redistribution. Therefore, the complex interaction between the OBC and CRC could be an important factor determining stream morphodynamics by promoting channel deepening.

[61] The half saddle point in the cross-sectional streamlines at the water surface coincides with the region of increased TKE that marks the outer bank shear layer. Turbulence in this region is highly anisotropic as most of the TKE is shown to be produced by transverse velocity fluctuations, presumably due to the lateral, low frequency flapping of the point where the OBC and CRC flows collide at the surface. Turbulence anisotropy is also shown to be important in several other regions within the channel, such as throughout the riffles and around the point bar. This finding has important implications for numerical simulations of turbulence in natural waterways pointing to the need for adopting turbulence models that can accurately account for the anisotropy of the Reynolds stresses.

[62] Horizontal large recirculation zones are observed along the inner bank of the bend. They consist of multiple recirculation eddies that span almost the entire area above the point bar. A striking finding in this regard is that the center of the primary recirculation eddy is located directly above the crest of the point bar, which points to the conclusion that recirculation zones play an important role in the formation of bars in alluvial streams.

[63] Finally, a major conclusion from our work as well as the recent study by *Kang et al.* [2011] is that the numerical simulation of flows in natural streams with arbitrarily complex bathymetry is now well within reach. A major challenge that still remains is undertaking high-resolution simulations of turbulence in large rivers and at full-scale Reynolds numbers. Computational algorithms such as the one we employed in this work coupled with the explosive growth of affordable computing power will make such simulations possible within the next few years.

[64] **Acknowledgments.** This work was supported by NSF grants EAR-0120914 (as part of the National Center for Earth-Surface Dynamics) and EAR-0738726 and a grant from Yonsei University, South Korea. Computational resources were provided by the University of Minnesota Supercomputing Institute. We are grateful to Anne Lightbody and Craig Hill for providing the experimental data of the bankfull flow in the Outdoor Stream-Lab. We would like to thank the editors and three anonymous reviewers for their helpful comments and suggestions, which improved the quality of this paper.

References

Abad, J. D., and M. H. Garcia (2009), Experiments in a high-amplitude Kinoshita meandering channel: 1. Implications of bend orientation on mean and turbulent flow structure, *Water Resour. Res.*, *45*, W02401, doi:10.1029/2008WR007016.

Bagnold, R. A. (1960), Some aspects of the shape of river meanders, *U.S. Geol. Surv. Prof. Pap.*, *282-E*, 135–144.

Bathurst, J. C., C. R. Thorne, and R. D. Hey (1979), Secondary flow and shear stress at river bends, *J. Hydraul. Div. Am. Soc. Civ. Eng.*, *105*(10), 1277–1295.

Blanckaert, K. (2009), Saturation of curvature-induced secondary flow, energy losses, and turbulence in sharp open-channel bends: Laboratory experiments, analysis, and modeling, *J. Geophys. Res.*, *114*, F03015, doi:10.1029/2008JF001137.

Blanckaert, K. (2010), Topographic steering, flow recirculation, velocity redistribution, and bed topography in sharp meander bends, *Water Resour. Res.*, *46*, W09506, doi:10.1029/2009WR008303.

Blanckaert, K., and H. J. de Vriend (2003), Non-linear modeling of mean flow redistribution in curved open channels, *Water Resour. Res.*, *39*(12), 1375, doi:10.1029/2003WR002068.

Blanckaert, K., and H. J. de Vriend (2004), Secondary flow in sharp open-channel bends, *J. Fluid Mech.*, *498*, 353–380, doi:10.1017/S0022112003006979.

Blanckaert, K., and H. J. de Vriend (2010), Meander dynamics: A nonlinear model without curvature restrictions for flow in open-channel bends, *J. Geophys. Res.*, *115*, F04011, doi:10.1029/2009JF001301.

Blanckaert, K., and W. Graf (2001), Mean flow and turbulence in open-channel bend, *J. Hydraul. Eng.*, *127*(10), 835–847, doi:10.1061/(ASCE)0733-9429(2001)127:10(835).

Blanckaert, K., A. Duarte, and A. J. Schleiss (2010), Influence of shallowness, bank inclination and bank roughness on the variability of flow patterns and boundary shear stress due to secondary currents in straight open-channels, *Adv. Water Resour.*, *33*, 1062–1074, doi:10.1016/j.advwatres.2010.06.012.

Bolla Pittaluga, M., G. Nobile, and G. Seminara (2009), A nonlinear model for river meandering, *Water Resour. Res.*, *45*, W04432, doi:10.1029/2008WR007298.

Cabot, W., and P. Moin (2000), Approximate wall boundary conditions in the large-eddy simulation of high Reynolds number flow, *Flow Turbul. Combust.*, *63*(1–4), 269–291, doi:10.1023/A:1009958917113.

Cotel, A. J., P. W. Webb, and H. Tritico (2006), Do brown trout choose locations with reduced turbulence?, *Trans. Am. Fish. Soc.*, *135*(3), 610–619, doi:10.1577/T04-196.1.

de Vriend, H. J. (1977), A mathematical model of steady flow in curved shallow channels, *J. Hydraul. Res.*, *15*, 37–54.

Dietrich, W. E., and J. D. Smith (1983), Influence of the point bar on flow through curved channels, *Water Resour. Res.*, *19*, 1173–1192, doi:10.1029/WR019i005p01173.

Dietrich, W. E., J. D. Smith, and T. Dunne (1979), Flow and sediment transport in a sand bedded meander, *J. Geol.*, *87*(3), 305–315, doi:10.1086/628419.

Engelhardt, C., A. Kruger, A. Sukhodolov, and A. Nicklisch (2004), A study of phytoplankton spatial distributions, flow structure and characteristics of mixing in a river reach with groynes. *J. Plankton Res.*, *26*(11), 1351–1366, doi:10.1093/plankt/fbh125.

Engelund, F. (1974), Flow and bed topography in channel bends, *J. Hydraul. Div. Am. Soc. Civ. Eng.*, *100*(11), 1631–1648.

Ferguson, R. I., D. R. Parsons, S. N. Lane, and R. J. Hardy (2003), Flow in meander bends with recirculation at the inner bank, *Water Resour. Res.*, *39*(11), 1322, doi:10.1029/2003WR001965.

Frothingham, K. M., and B. L. Rhoads (2003), Three-dimensional flow structure and channel change in an asymmetrical compound meander loop, Embarras River, Illinois, *Earth Surf. Processes Landforms*, *28*(6), 625–644, doi:10.1002/esp.471.

Ge, L., and F. Sotiropoulos (2007), A numerical method for solving the 3D unsteady incompressible Navier-Stokes equations in curvilinear domains with complex immersed boundaries, *J. Comput. Phys.*, *225*(2), 1782–1809, doi:10.1016/j.jcp.2007.02.017.

Germano, M., U. Piomelli, P. Moin, and W. H. Cabot (1991), A dynamic subgrid-scale eddy viscosity model, *Phys. Fluids A*, *3*(7), 1760–1765, doi:10.1063/1.857955.

Gilmanov, A., and F. Sotiropoulos (2005), A hybrid Cartesian/immersed boundary method for simulating flows with 3D, geometrically complex, moving bodies, *J. Comput. Phys.*, *207*(2), 457–492, doi:10.1016/j.jcp.2005.01.020.

Hey, R. D., and C. R. Thorne (1975), Secondary flows in river channels, *Area*, *7*, 191–195.

Hondzo, M., and A. Wüest (2009), Do microscopic organisms feel turbulent flows?, *Environ. Sci. Technol.*, *43*(3), 764–768, doi:10.1021/es801655p.

Huisman, J., M. Arrayás, U. Ebert, and B. Sommeijer (2002), How do sinking phytoplankton species manage to persist?, *Am. Nat.*, *159*(3), 245–254, doi:10.1086/338511.

Humphrey, J. A. C., J. H. Whitelaw, and G. Yee (1981), Turbulent flow in a square duct with strong curvature, *J. Fluid Mech.*, *103*, 443–463, doi:10.1017/S0022112081001419.

Jamieson, C., G. Post, and C. D. Rennie (2010), Spatial variability of three-dimensional Reynolds stresses in a developing channel bend, *Earth Surf. Processes Landforms*, *35*(9), 1029–1043, doi:10.1002/esp.1930.

Johannesson, H., and G. Parker (1989), Secondary flow in mildly sinuous channel, *J. Hydraul. Eng.*, *115*(3), 289–308, doi:10.1061/(ASCE)0733-9429(1989)115:3(289).

Kalkwijk, J. P. T., and H. J. de Vriend (1980), Computation of the flow in shallow river bends, *J. Hydraul. Res.*, *18*(4), 327–342, doi:10.1080/00221688009499539.

Kang, S., A. Lightbody, C. Hill, and F. Sotiropoulos (2011), High-resolution numerical simulation of turbulence in natural waterways, *Adv. Water Resour.*, *34*(1), 98–113, doi:10.1016/j.advwatres.2010.09.018.

Keller, E. A. (1971), Areal sorting of bed-load material: The hypothesis of velocity reversal, *Geol. Soc. Am. Bull.*, *82*, 753–756, doi:10.1130/0016-7606(1971)82[753:ASOBMT]2.0.CO;2.

Keller, E. A. (1972), Development of alluvial stream channels: A five-stage model, *Geol. Soc. Am. Bull.*, *83*, 1531–1536, doi:10.1130/0016-7606(1972)83[1531:DOASCA]2.0.CO;2.

Le, H., P. Moin, and J. Kim (1997), Direct numerical simulation of turbulent flow over a backward-facing step, *J. Fluid Mech.*, *330*, 349–374, doi:10.1017/S0022112096003941.

Leeder, M. R., and P. H. Bridges (1975), Flow separation in meander bends, *Nature*, *253*, 338–339, doi:10.1038/253338a0.

Leopold, L. B., and M. G. Wolman (1960), River meanders, *Geol. Soc. Am. Bull.*, *71*, 769–793, doi:10.1130/0016-7606(1960)71[769:RM]2.0.CO;2.

Leopold, L. B., R. A. Bagnold, M. G. Wolman, and L. M. Brush (1960), Flow resistance in sinuous and irregular channels, *U.S. Geol. Surv. Prof. Pap.*, *282D*, 111–134.

Lohrmann, A., R. Cabrera, and N. C. Kraus (1994), Acoustic-Doppler velocimeter (ADV) for laboratory use, in *Fundamentals and Advancements in Hydraulic Measurements and Experimentation*, edited by C. A. Pugh, pp. 351–365, Am. Soc. of Civ. Eng., New York.

Lumley, J. L. (1978), Computational modelling of turbulent flows, *Adv. Appl. Mech.*, *18*, 126–176.

Moffatt, H. K. (1969), The degree of knottedness of tangled vortex lines, *J. Fluid Mech.*, *35*(1), 117–129, doi:10.1017/S0022112069000991.

Nanson, G. C. (1980), Point bar and floodplain formation of the meandering Beatton River, northeastern British Columbia, Canada, *Sedimentology*, *27*(1), 3–29, doi:10.1111/j.1365-3091.1980.tb01155.x.

Nikora, V. I., and D. G. Goring (1998), ADV measurements of turbulence: can we improve their interpretation?, *J. Hydraul. Eng.*, *124*(6), 630–634, doi:10.1061/(ASCE)0733-9429(1998)124:6(630).

Naot, D. (1984), Response of channel flow to roughness heterogeneity, *J. Hydraul. Eng.*, *110*(11), 1568–1587, doi:10.1061/(ASCE)0733-9429(1984)110:11(1568).

Perkins, H. J. (1970), The formation of streamwise vorticity in turbulent flow, *J. Fluid Mech.*, *44*(4), 721–740, doi:10.1017/S0022112070002112.

Reynolds, C. S. (2000), Hydroecology of river plankton: The role of variability in channel flow, *Hydrol. Processes*, *14*, 3119–3132, doi:10.1002/1099-1085(200011/12)14:16/17<3119::AID-HYP137>3.0.CO;2-6.

Rozovskii, I. L. (1957), *Flow of Water in Bends of Open Channels*, Acad. of Sci. of the Ukr. SSR, Kiev.

Rubin, D. M., J. C. Schmidt, and J. N. Moore (1990), Origin, structure, and evolution of a reattachment bar, Colorado River, Grand Canyon, Arizona, *J. Sediment. Res.*, *60*(6), 982–991.

Schmidt, J. C. (1986), Changes in alluvial deposits, upper grand canyon, in *Proceedings of the Fourth Federal Interagency Sedimentation Conference*, vol. 2, pp. 48–57, U.S. Geol. Surv., Reston, Va.

Schmidt, J. C. (1990), Recirculating flow and sedimentation in the Colorado River in Grand Canyon, Arizona, *J. Geol.*, *98*(5), 709–724.

Stoesser, T., N. Ruether, and N. R. B. Olsen (2010), Calculation of primary and secondary flow and boundary shear stresses in a meandering channel, *Adv. Water Resour.*, *33*, 158–170, doi:10.1016/j.advwatres.2009.11.001.

Thompson, A. (1986), Secondary flows and the pool-riffle unit: A case study of the processes of meander development, *Earth Surf. Processes Landforms*, *11*(6), 631–641, doi:10.1002/esp.3290110606.

Thomson, J. (1876), On the origin of windings of rivers in alluvial plains, with remarks on the flow of water round bends in pipes, *Proc. R. Soc. London*, *25*, 5–8.

Thorne, C. R., L. W. Zevenbergen, J. C. Pitlick, S. Rais, J. B. Bradley, and P. Y. Julien (1985), Direct measurements of secondary currents in a meandering sand-bed river, *Nature*, *315*, 746–747, doi:10.1038/315746a0.

Tobak, M., and D. J. Peake (1982), Topology of three-dimensional separated flows, *Annu. Rev. Fluid Mech.*, *14*(1), 61–85, doi:10.1146/annurev.fl.14.010182.000425.

Tominaga, A., I. Nezu, K. Ezaki, and H. Nakagawa (1989), Three-dimensional turbulent structure in straight open channel flows, *J. Hydraul. Res.*, *27*, 149–173, doi:10.1080/00221688909499249.

van Balen, W., W. S. J. Uijttewaal, and K. Blanckaert (2009), Large-eddy simulation of a mildly curved open-channel flow, *J. Fluid Mech.*, *630*, 413–442, doi:10.1017/S0022112009007277.

van Balen, W., K. Blanckaert, and W. S. J. Uijttewaal (2010a), Analysis of the role of turbulence in curved open-channel flow at different water depths by means of experiments, LES and RANS, *J. Turbul.*, *11*, 1–34, doi:10.1080/14685241003789404.

van Balen, W., K. Blanckaert, and W. S. J. Uijttewaal (2010b), Large-eddy simulation of a curved open-channel flow over topography, *Phys. Fluids*, *22*, 075108, doi:10.1063/1.3459152.

Van Bendegom, L. (1947), Some considerations on river morphology and river improvement [in Dutch], *De Ingenieur*, *59*, 1–11. [English translation, *Tech. Transl. 1054*, Natl. Res. Counc. Can., Ottawa, 1963.]

Vanoni, V. A. (1975), *Sedimentation Engineering*, Am. Soc. of Civ. Eng., New York.

Wang, M., and P. Moin (2002), Dynamic wall modeling for large-eddy simulation of complex turbulent flows, *Phys. Fluids*, *14*(7), 2043–2051, doi:10.1063/1.1476668.

S. Kang and F. Sotiropoulos, St. Anthony Falls Laboratory, Department of Civil Engineering, University of Minnesota, 2 Third Ave. SE, Minneapolis, MN 55414, USA. (fotis@umn.edu)